Thesis for the degree of Doctor of Philosophy

Reaction kinetics of NH$_3$-SCR over Cu-CHA from first principles

Yingxin Feng

Department of Physics

CHALMERS UNIVERSITY of TECHNOLOGY

Göteborg, Sweden 2024

Reaction kinetics of NH$_3$-SCR over Cu-CHA from first principles

Yingxin Feng
Department of Physics
Chalmers University of Technology

Abstract

Ammonia-assisted selective catalytic reduction (NH$_3$-SCR) is an advanced technology to reduce nitrogen oxide (NO$_x$) emissions from lean-burn engines. NH$_3$ is added to the exhaust gas and reacts selectively with NO$_x$, forming N$_2$ and H$_2$O. Small-pore Cu-exchanged chabazite (Cu-CHA) is a widely used zeolite-based catalyst for NH$_3$-SCR thanks to its high activity, high selectivity, and durability. However, one issue is the formation of small amounts of nitrous oxide (N$_2$O), which is a strong greenhouse gas. Atomic level understanding is valuable to improve the performance of NH$_3$-SCR catalyst and meet the increasingly stringent emission standards.

The state of Cu-CHA during NH$_3$-SCR reaction depends sensitively on the reaction temperature. At low temperatures, Cu-ions are solvated by NH$_3$, forming Cu(NH$_3$)$_2^+$ complexes, while framework-bound Cu dominates at high temperatures. Experimentally, a non-monotonic behavior in NO conversion is observed with increasing temperature, which reflects a change in the active site.

In this thesis, NH$_3$-SCR over Cu-CHA is investigated using density functional theory (DFT) calculations and kinetic simulations. In the low-temperature range ($<250°$C), a pair of Cu(NH$_3$)$_2^+$ is required for O$_2$ adsorption to form a Cu-peroxo complex, which is a key Cu-intermediate. The reaction intermediates HONO and H$_2$NNO can be converted to N$_2$ and H$_2$O over Brønsted acid sites. H$_2$NNO is found to be the origin of N$_2$O formation when decomposing over Cu-peroxo species. At high-temperature ($>350°$C), the proposed reaction mechanism suggests that the reaction proceeds over single framework Cu sites and starts from the co-adsorption of O$_2$ and NO. The main source of N$_2$O formation at high temperatures is suggested to be ammonium nitrate decomposition. By combining the reaction mechanisms for high and low temperatures, the non-monotonic temperature-dependent reaction activity is successfully reproduced.

The present work deepens the understanding of the reaction mechanism of NH$_3$-SCR on Cu-CHA in a wide temperature range and provides theoretical support for further improvement of the catalyst performance.

Keywords: Catalysis, density functional theory, microkinetic modeling, Cu-CHA, ammonia assisted selective catalytic reduction

List of Publications

This thesis is based on the following appended papers:

I. The Role of H$^+$- and Cu$^+$-Sites for N$_2$O Formation during NH$_3$-SCR over Cu-CHA
Y. Feng, T.V.W. Janssens, P.N.R. Vennestrøm, J. Jansson, M. Skoglundh and H. Grönbeck
The Journal of Physical Chemistry C, **125** (2021), 4595-4601

II. A First-Principles Microkinetic Model for Low-Temperature NH$_3$ Assisted Selective Catalytic Reduction of NO over Cu-CHA
Y. Feng, X. Wang, T.V.W. Janssens, P.N.R. Vennestrøm, J. Jansson, M. Skoglundh and H.Grönbeck
ACS Catalysis, **11** (2021), 14395–14407

III. Simplified Kinetic Model for NH$_3$-SCR Over Cu-CHA Based on First-Principles Calculations
Y. Feng, D. Creaser and H. Grönbeck
Topic in Catalysis, **66** (2023), 743–749

IV. High-Temperature Reaction Mechanism of NH$_3$-SCR over Cu-CHA: One or Two Copper Ions?
Y. Feng, T.V.W. Janssens, P.N.R. Vennestrøm, J. Jansson, M. Skoglundh and H. Grönbeck
Submitted

V. Kinetic Monte Carlo Simulation Elucidates the Effect of Al-Distribution for Low-Temperatures NH$_3$-SCR over Cu-CHA
Y. Feng, and H. Grönbeck
In manuscript

VI. Range-Separated Hybrid van der Waals Density Functional to Describe Cu$_2$O$_2$-Complexes
C. Frostenson, Y. Feng, P. Hyldgaard and H. Grönbeck
Submitted

VII. *In Situ* DRIFT Studies on N$_2$O Formation over Cu-Functionalized Zeolites during Ammonia-SCR
G. Isapour, A. Wang, J. Han, Y. Feng, H. Grönbeck, D. Creaser, L. Olsson, M. Skoglundh, and H. Härelind
Catalysis Science & Technology, **12** (2022), 3921-3936

My contributions to the publications

Paper I
I performed all the calculations. I wrote the first draft of the paper, which was finalized together with my co-authors.

Paper II
I programmed the code for the microkinetic modeling and performed all the DFT calculations and kinetic simulations. I wrote the first draft of the paper, which was finalized together with my co-authors.

Paper III
I programmed the code for the microkinetic modeling and performed all the DFT calculations and kinetic simulations. I wrote the first draft of the paper, which was finalized together with my co-authors.

Paper IV
I programmed the code for the microkinetic modeling and performed all the DFT calculations and kinetic simulations. I wrote the first draft of the paper, which was finalized together with my co-authors.

Paper V
I performed all the kinetic Monte Carlo simulations and the DFT calculations. I wrote the first draft of the manuscript, which was finalized together with my co-author.

Paper VI
I performed the DFT calculations using VASP and co-authored that part of the manuscript.

Paper VII
I performed all the DFT calculations and wrote the parts related to my calculations.

Contents

Chapter 1

Introduction

'Reducing environmental impact will require entirely new catalysts: catalysts for new processes, more active and more selective catalysts and preferably catalysts that are made from earth-abundant elements.' J. K. Nørskov (2009)[1]

Our society relies on efficient transportation of people and goods. At present, the transportation system is based on combustion of liquid fossil fuels,[2] which is connected to emission of pollutants, such as nitrous oxide (NO_x), hydrocarbons (HC), and carbon monoxide (CO) that need to be controlled.[3] Moreover, combustion of carbon-based fuels results in carbon dioxide (CO_2), which is a greenhouse gas.[4] Thus, within a carbon-based transportation system, fuel efficiency should be maximized to limit CO_2 emission. Thanks to the progress of engine technology, the emissions of modern engines have been greatly reduced as compared to the 1970s.[5–7] More importantly, the utilization of after-treatment technologies has played an integral role in further reducing the emissions.[7;8] The current challenge within after-treatment research is, to meet increasingly rigorous emission standards,[9] and simultaneously improve fuel efficiency.[7]

The technology to control exhaust from stoichiometric combustion is the three-way catalyst (TWC). TWCs are efficient and the application of TWC was a huge step forward for the emission control of gasoline engines. With the TWC, CO, and HC are oxidized to CO_2 and H_2O, while NO_x is reduced to N_2 as shown in Figure 1.1.[10;11]
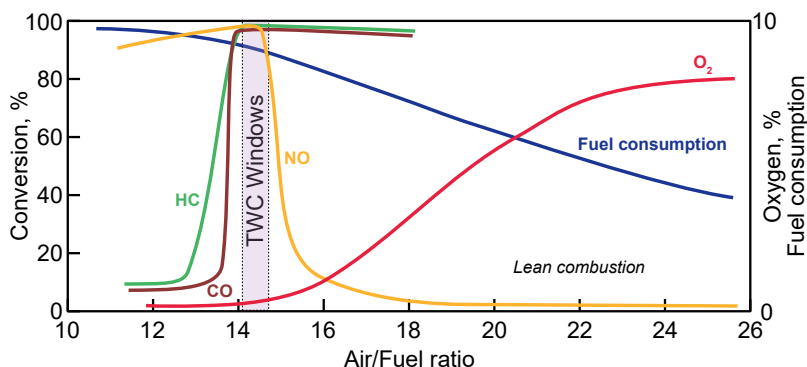

Figure 1.1: Conversion of NO, HC, and CO together with fuel consumption for a TWC as a function of the air-to-fuel ratio. The figure is adapted from the book written by B. Pereda-Ayo *et al.*[12(p. 164)]

In a typical TWC, the reactions occur over nanoparticles of noble metals, composed of Pt, Pd, and Rh supported on a high surface area Al_2O_3, which is stabilized by barium

and/or lanthanum oxides. CeO_2–ZrO_2 mixed oxides are, moreover, added as oxygen storage materials and promoters.[13]. TWC has an obvious deficiency in that, it needs to operate under stoichiometric conditions (air-to-fuel ratio of ≈ 14.7), which limits fuel efficiency.

In recent years, lean-burn engines where oxygen is in excess have been widely used owing to their higher fuel efficiency.[10] Under the lean-burn conditions with high air/fuel ratios, most of the fuel can be fully combusted into CO_2 and only a minimal amount of CO and HC is emitted. NO_x is, however, still emitted as it forms at high temperatures in the combustion process from oxygen and nitrogen in the air. Therefore, there is an urgent need for catalysts that can selectively reduce NO_x in oxygen excess.

Ammonia assisted selective catalytic reduction (NH_3-SCR) is currently used for NO_x reduction in O_2 excess.[14] NO_x is in this technology reduced to N_2 using NH_3 as reducing agent.

1.1 Heterogeneous catalysis

In general, catalysis is a process that accelerates the rate of chemical reactions with the assistance of a substance, the catalyst, which is not consumed during the reaction. By offering alternative and energetically favorable mechanisms, catalysts enable the reactions to proceed under more accessible conditions as compared to the non-catalyzed situation.[15 (p.2-4)] Note that the catalyst does not change the thermodynamics of the reaction. Catalysts can be divided into three main categories, namely heterogeneous catalyst, homogeneous catalyst, and enzymatic catalyst. Among them, heterogeneous catalysts are the most widely used in industrial applications, and solid catalysts are used in about 90% of all chemical processes.[16]

Catalysts facilitate reactions by providing active sites that promote the breaking of bonds within the reactants and the generating of new bonds for the formation of products. For heterogeneous catalysts, the active sites are usually at the surface of a solid and it is desirable to maximize the number of active sites per reactor volume by increasing the specific surface area of the catalyst. Therefore, as for the TWC catalysts, a heterogeneous catalyst is generally composed of an active substance and supported by a high surface area substrate. As the reactants/products and the catalyst are in different phases, heterogeneous catalysts have the advantage that the reactants, and products are easily separated from the catalyst. On the contrary, in homogeneous catalysis, the catalysts and reactants are both in the gas phase or the liquid phase. Because of the full contact with the reactants, homogeneous catalyst exhibits high catalytic efficiency. Moreover, its uniform active site can result in high selectivity. According to these strengths, homogeneous catalysts are used extensively in chemical and pharmaceutical production,[17] despite the difficulty of separating catalysts and products.

In recent years, single-atom catalysts and metal-exchange zeolite catalysts have received wide attention and have been the subject of extensive research.[18;19] By dispersing metals into atoms or forming homogeneous complexes, catalysts can obtain properties similar to homogeneous catalysts while maintained in the solid phase.[19;20] By this way, linking homo- and heterogeneous catalysis, it is anticipated that the selectivity and activity of heterogeneous catalysts can be improved.

1.2 Ammonia assisted selective catalytic reduction

Nitrogen oxide (NO_x) is an undesirable byproduct during fuel combustion, which is formed from N_2 and O_2 in the air. NO_x emission should be controlled as it contributes to the formation of smog and acid rain.[21;22] In the field of NO_x abatement, NH_3-SCR is the leading technology for NO_x reduction in oxygen excess thanks to efficiency, selectivity, and economy.[21] Depending on the NO/NO_x ratio, the reaction is typically considered to occur via the overall schemes for standard-, fast-, or NO_2-SCR.[14;23;24]

As NO_x emissions from diesel engines are dominated by NO and contain only a small amount of NO_2,[25] the standard-SCR reaction that only involve NO, NH_3 and O_2 is considered to be the primary reaction path:

$$4\,NH_3 + 4\,NO + O_2 \rightarrow 4\,N_2 + 6\,H_2O \tag{1.1}$$
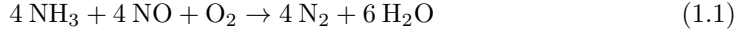
One NH_3 molecule is needed per NO, and O_2 is required to accommodate the H-atoms. If the content of NO_2 increases until the ratio of NO and NO_2 approaches 1:1, the reaction can occur according to the fast-SCR scheme:

$$2\,NH_3 + NO + NO_2 \rightarrow 2\,N_2 + 3\,H_2O \tag{1.2}$$
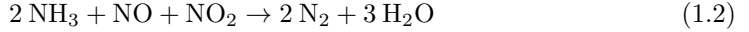
The NH_3/NO_x stoichiometry is one and the fast-SCR reaction does not require O_2. In the cases where the amount of NO_2 is more than twice of NO, the NO_2-SCR reaction that only requires NO_2 and NH_3 can be active:

$$8\,NH_3 + 6\,NO_2 \rightarrow 7\,N_2 + 12\,H_2O \tag{1.3}$$
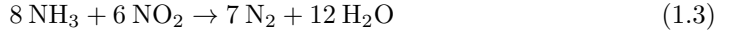
The stoichiometry of the NO_2-SCR reaction requires an excess of NH_3.

The sketched reactions are ideal overall NH_3-SCR reactions as they consume NO_x and fully convert them into N_2 and H_2O. However, depending on the reaction conditions, a variety of side reactions can occur and produce undesirable byproducts, for example, nitrous oxide (N_2O).

1.2.1 N_2O formation during NH_3-SCR

N_2O, a byproduct of NH_3-SCR reaction, is undesirable as it strongly contributes to the greenhouse effect and ozone layer depletion.[26] N_2O has been reported to account for 2.6-8.3% of total tailpipe CO_2 equivalent emissions for heavy-duty diesel vehicles.[27] According to its powerful greenhouse effect and the stringent requirements for N_2O emissions in the new standard of emissions from heavy-duty vehicles (Euro VII)[28], the emission of N_2O from diesel vehicles should be controlled.

There are different suggestions regarding the mechanism for N_2O formation during NH_3-SCR. Isotope labeling experiments revealed that the two N atoms in N_2O are formed from NH_3 and NO.[27] It is, therefore, reasonable to assume that the formation of N_2O originates from the incomplete NO_x reduction in the NH_3-SCR reaction.

It is currently assumed that under NH_3-SCR reaction conditions, NH_3 can react with surface nitrates forming ammonium nitrate (NH_4NO_3) over the catalysts.[29] NH_4NO_3 can further decompose into N_2O and H_2O, which is the proposed source of N_2O:[29;30]

$$NH_4NO_3 \rightarrow N_2O + 2\,H_2O \tag{1.4}$$

The thermal decomposition of NH_4NO_3 into N_2O in the gas phase occurs at temperatures above 290 °C.[31;32] However, the formation of N_2O during NH_3-SCR usually begins at lower temperatures[33;34] and its reaction mechanism is not clear.

To fulfill the demand for applications and to restrain the reaction to the preferred direction, understanding of the reaction mechanism is important to improve the catalyst performance.

1.3 Catalysts for NH_3-SCR

To be a proper NH_3-SCR catalyst with sufficient activity at the conditions of application, some requirements need to be met. First, the catalyst should be able to promote the H_3N-NO coupling between NO_x and NH_3 while allowing the scission of the N-H bond. The catalyst should preferably not completely decompose NH_3 into N and H, as this may promote the oxidation of N that forms additional NO_x. Thus, a good NH_3-SCR catalyst usually has high dispersion of active site and preference for N-N coupling, making the reaction highly selective for N_2 formation rather than NO oxidation. Second, the oxidation state of the active sites should be able to change, which allows the activation of O_2 that is needed to accommodate the H from NH_3 by forming water. Since a certain amount of sulfur oxide (SO_x) can be present in the exhaust gas, the catalyst should be resistant to SO_x poisoning. In addition, the catalyst also needs to be tolerant to hydrothermal aging due to the presence of water and the potentially high temperatures during operation.

According to the high thermal mass, the temperature before the SCR catalyst could be up to 300 °C.[14] However, to achieve better performance and be applicable at different conditions, especially during the cold start period, it is desirable to achieve high activity in a temperature window from 150 to 300 °C. Currently, vanadia-based catalysts and Fe/Cu-exchanged zeolite catalysts are the main types of catalysts that are utilized for NH_3-SCR, as they fulfill the desired requirements.

1.3.1 Vanadia-based catalysts

Vanadia-based catalysts are common and were early commercialized for NH_3-SCR. Generally, vanadia-based catalysts contain 1∼3% of V_2O_5 as the active component dispersed on a TiO_2 support. 10% of WO_3 is typically added as a promoter.[14;35] Compared with metal-exchanged zeolite, which is the other common SCR catalyst, the vanadium-based catalyst has a stronger resistance to sulfur poisoning.[36] However, it shows relatively poor low-temperature performance and weak high-temperature durability. Moreover, a small amount of vanadium can be emitted from the catalyst during high-temperature operations, for example, during the combustion of coal and heavy fuel oil in industrial combustors.[37] The emitted vanadium compounds, especially vanadium pentoxide (V_2O_5), are hazardous or carcinogenic and should, thus, be controlled.[37] As typical for a heterogeneous catalyst, research on vanadia-based catalysts mainly focuses on the characterization of the active site and the reaction mechanism, to achieve better catalytic performance by doping other elements or surface modification.

1.3.2 Fe/Cu-exchanged zeolite catalysts

Metal-exchanged (mostly Cu and Fe) zeolites are appropriate catalysts of NH_3-SCR and their performance has markedly improved during the last decades.[14] The main advantages of metal-exchange zeolites are that they have better hydrothermal stability than vanadia-based catalysts and show a high NO_x conversion over a wide temperature window.[14;24;38]

Zeolites are crystalline porous aluminosilicates that exist naturally and can also be synthesized.[39] In Fig. 1.2, the structure of SSZ-13 is shown as an example. The Si^{4+} and Al^{3+} are in the structure tetrahedrally coordinated to oxygen cations, providing a negatively charged environment that can be balanced by a proton or metal cations (i.e Cu^+). In this way, metal sites and Brønsted acid sites can exist in the zeolites together as a multi-site system.[40] The ratio of metal sites and Brønsted acid sites in the system can also be controlled by adjusting the Si/Al ratio and the loading of metal cations, resulting in a highly adjustable catalyst. The highly dispersed metal cations give ions-exchanged zeolite catalysts the characteristics of homogeneous catalysis during the NH_3-SCR environments.[19]
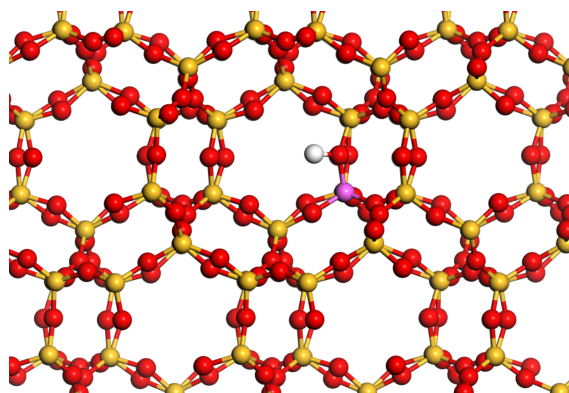
Figure 1.2: Framework structure of SSZ-13 with one Si atom has been replaced with Al. Atomic color codes: H (white), O (red), Si (yellow), and Al (pink).

The pore size of the zeolites has been found to have a significant effect on the catalytic performance. Zeolites that have varying structures and pore sizes, such as MOR, FER, BEA, ZSM-5, and SSZ-13 have been studied to reveal a relationship between catalytic performance and zeolite structural properties.[41;42] It has been shown that zeolites with small pore sizes give a better activity and selectivity for NH_3-SCR.[42;43] When comparing the hydrothermal stability, low-temperature activity and N_2 selectivity of NH_3-SCR, Cu-SSZ-13 with a chabazite structure (hereinafter referred to as Cu-CHA) is generally superior to other catalysts.[14;42;44;45] According to its excellent NO_x reduction activity, Cu-CHA has been commercialized.[24;43] However, despite its good catalytic properties, further research and improvement over Cu-CHA is necessary to meet the increasingly stringent emission standards worldwide.

The detailed catalytic mechanisms of NH_3-SCR over Cu-CHA have been studied and

debated over the past years. At present, based on *in situ* X-ray absorption spectroscopy experiments and density functional theory calculations, it is generally accepted that NH$_3$-SCR reaction at low temperatures proceeds via redox steps over mobile Cu species. [46;47] During this reaction, the Cu ions are reduced from Cu(II) to Cu(I) and oxidized back to Cu(II) by O$_2$ adsorption.

During the NH$_3$-SCR over Cu-CHA with Cu-loading of 0.5 to 6%, the emission of N$_2$O is located between 150 to 250 °C, and the emission peak is at about 200 °C. [48;49] In addition, by comparing samples with different Cu-loadings, it can be seen that the selectivity of N$_2$O increases with higher Cu-loading, which indicates that when a sufficient amount of copper is in the catalyst, N$_2$O can be generated via a low-energy barrier pathway that is related to Cu. The above observations suggest that the presence of Cu may also contribute to the production of N$_2$O. To reduce the emission of N$_2$O, it is necessary to investigate the reaction mechanism of N$_2$O formation over Cu-CHA during NH$_3$-SCR.

1.4   Objectives

The objective of this work is to explore the catalytic mechanism of N$_2$O formation during NH$_3$-SCR over Cu-CHA, provide mechanistic understandings of NH$_3$-SCR at different temperatures and establish a link between theoretical calculations and experiments through kinetic modeling. By understanding the reaction mechanism and studying the relationship between catalytic performance and material properties, the ultimate goal is to be able to design Cu-CHA catalysts rationally and obtain better catalytic performance such as lower light-off temperature, higher activity and higher selectivity to N$_2$.

In **Paper I**, the formation of N$_2$O over gas-phase, Al-free CHA and H-CHA from NH$_4$NO$_3$ decomposition was explored by first principles calculations. The comparison between Al-free and H-CHA shows that Brønsted acid site can promote the decomposition process. More importantly, a novel path for N$_2$O formation via H$_2$NNO decomposition in Cu-CHA was suggested.

In **Paper II**, a first principles microkinetic model was constructed to investigate low-temperature NH$_3$-SCR over Cu-CHA. The proposed multisite reaction, where the active sites are Cu-peroxo complex and Brønsted acid site is used, and the alternative steps as well as the N$_2$O formation path based on **Paper I** is included in the microkinetic model. The comparison between experiments and the kinetic modeling result revealed the critical effect of NH$_3$-blocking of Cu-peroxo on the reaction kinetics. The calculated values for activation energy and reaction orders based on the model show a good agreement with the experimental data. Moreover, a degree of rate control analysis reveals how the rate-controlling step changes with temperatures and gives unique insights into the function of Cu-CHA catalysts for NH$_3$-SCR.

In **Paper III**, based on the detailed microkinetic model developed in **Paper II**, a simplified microkinetic model was designed. In the simplified model, only the elementary steps that have a decisive influence on the reaction rate are retained, while the others are lumped. By fitting lumped kinetic parameters to the detailed model, the simplified model reproduces the results of N$_2$ and N$_2$O formation from the detailed model with high accuracy using only five reaction steps.

In **Paper IV**, the reaction mechanism and kinetics of NH_3-SCR over Cu-CHA at high-temperature were investigated and discussed. At high temperatures, the mobile $[Cu(NH_3)_2]^+$ complexes that are present in the low-temperature mechanism decompose. DFT simulation revealed that at high temperatures the reaction is performed over single framework bound Cu-ions. By combining the high- and low-temperature kinetic model with the coverage of mobile $[Cu(NH_3)_2]^+$ complexes at different temperatures, the characteristic "seagull" profile of the NH_3-SCR activity with a local minimum at intermediate temperatures is reproduced. This work provides a detailed atomistic understanding of the role and transformation of mobile and framework forms of Cu-ions during standard SCR in Cu-CHA at different temperatures.

In **Paper V**, kinetic Monte Carlo simulations are used to investigate the effect of Al-distribution on low-temperature NH_3-SCR over Cu-CHA. Al-distribution is found to impact the stability of $[Cu(NH_3)_2]^+$ pairs and the competitive NO/NH_3 adsorption, which determines the NH_3-SCR reaction rate. This work successfully linked catalytic performance with Al-distribution and provided a computational basis for further development of the Cu-CHA materials.

Paper VI is a systematic study of the description of activated O_2 in Cu-CHA. Cu-peroxo complex is the key intermediate in the NH_3-SCR reaction over Cu-CHA. The description of the peroxo complex is challenging due to the localized Cu 3d-states and the vdW interaction between the complex and the zeolite framework. Here, we investigated the performance of different density functionals.

In **Paper VII**, DFT calculations were performed to assist the assignments of the results from *In situ* DRIFTS. By comparing the simulated vibrations of O-H and N-O bonds at different CHA sites, DFT calculations provide a reasonable interpretation of the DRIFT spectrum and reveal the potential species during the NO oxidation step. This work shows the important role of DFT calculations in assisting with spectrum analysis, especially of systems that have complex structures and extensive adsorption sites.

This thesis which in part is based on my licentiate thesis,[50] shows that it is possible to connect experimental and theoretical catalysis in a direct manner. With this approach, the complex catalytic processes of NH_3-SCR have been clarified and theoretical guidance can be used to promote the catalytic performance of Cu-CHA. The present work is expected to contribute to the development of exhaust gas after-treatment systems to meet stringent emission standards.

Chapter 2

Electronic structure calculations

'The underlying physical laws necessary for the mathematical theory of a large part of physics and the whole of chemistry are thus completely known, and the difficulty is only that the exact application of these laws leads to equations much too complicated to be soluble. It therefore becomes desirable that approximate practical methods of applying quantum mechanics should be developed, which can lead to an explanation of the main features of complex atomic systems without too much computation.' Paul Dirac (1929)[51].

The calculation of the electronic structure to obtain the electronic energy is the starting point for first principles simulations of chemical transformations. The Schrödinger equation is the cornerstone, and how to solve this many-body equation properly is a long-standing challenge. Due to the difficulty of expressing exact solutions, approximations have evolved over the years. The Hartree-Fock theory, which is the starting point for wave function based methods, and the density functional theory (DFT) are the two main approaches for obtaining electronic energy. The calculations in this thesis are performed using DFT, and the foundations, as well as, developments of DFT will be presented in this chapter.

2.1   The Schrödinger equation

The total energy of a set of electrons and nuclei is within quantum mechanics described by the Schrödinger equation:[52]

$$\hat{H}\Psi = E\Psi \tag{2.1}$$

Where $\hat{H}$ is the Hamiltonian operator corresponding to the total energy of the system and Ψ is the wave function. In the absence of magnetic or electric fields, the $\hat{H}$ for a many-body system of n nuclei and n_e electrons is given by:

$$\hat{H} = \sum_{\alpha}^{n} \left[-\frac{\nabla_{R_\alpha}^2}{2M_\alpha} + \frac{1}{2} \sum_{\alpha,\alpha>\beta}^{n} \frac{Z_\alpha Z_\beta}{|R_\alpha - R_\beta|} \right] + \sum_{i}^{n_e} \left[-\frac{\nabla_{r_i}^2}{2} + \frac{1}{2} \sum_{i,i>j}^{n_e} \frac{1}{|r_i - r_j|} \right]$$
$$- \frac{1}{2} \sum_{i}^{n_e} \sum_{\alpha}^{n} \frac{Z_\alpha}{|r_i - R_\alpha|} \tag{2.2}$$

Hartree atomic units ($e = m_e = \hbar = \frac{1}{4\pi\varepsilon_0} = 1$) are used in this equation. Here, the first term is the nuclei kinetic energy and nuclei-nuclei interaction ($\hat{H}_{nn}$), the second term is the electron kinetic energy and electron-electron interaction ($\hat{H}_{ee}$), and the last term is

the nuclei-electron interaction ($\hat{H}_{ne}$). Thus, the many-body Hamiltonian can be written as:

$$\hat{H} = \hat{H}_{nn} + \hat{H}_{ee} + \hat{H}_{ne} \tag{2.3}$$

2.2 The Born-Oppenheimer approximation

Although the Schrödinger equation describes the many-body system, it can only be solved analytically for one-electron systems, for example, a hydrogen atom consisting of one electron and one proton. To simplify the many-body problem, the Born-Oppenheimer approximation,[53] which is based on the large difference in the mass and speeds of electrons and nuclei, is generally the first approximation. Here, the electronic and nuclear wavefunctions are separated. As electrons are much lighter and move much faster than nuclei, it is possible to neglect the motion of the nuclei while treating the electrons as moving in the electrostatic field created by the nuclei. Following the Born-Oppenheimer approximation, the many-body Hamiltonian $\hat{H}$ can be separated into the electronic Hamiltonian $\hat{H}_e$ and nuclei Hamiltonian $\hat{H}_n$. The electronic Hamiltonian $\hat{H}_e$ is:

$$\hat{H}_e = \hat{H}_{ee} + \hat{H}_{ne} = \hat{T} + \hat{V}_{ee} + \hat{V}_{ext} \tag{2.4}$$

Where $\hat{T}$ is the kinetic energy operator for the electrons, $\hat{V}_{ee}$ is the electron-electron interactions, and $\hat{V}_{ext}$ is the external potential of the nuclei field. The Born-Oppenheimer approximation simplifies the Schrödinger equation, but it still can not be solved exactly for systems with many electrons. The reason here is the electron-electron interactions, which remain a many-body problem.

2.3 The density functional theory

To bring Schrödinger equation into practical use, different methods have been developed to actually solve the many-electron problem. One of the most widely used approaches today is DFT, which is based on the Hohenberg-Kohn theorems.[54] The Hohenberg-Kohn theorems state that the ground-state density is a unique functional of the external potential $\hat{V}_{ext}$ and that the ground-state energy can be determined by $\hat{V}_{ext}$. Thus, the energy and the intricate many-body effects of the system can be described by the electron density.[55]

2.3.1 The Kohn-Sham formulation

Although the Hohenberg-Kohn theorem connects the electron density and the energy of the system by an energy functional, the exact form of the functional is still unknown. With the introduction of one electron orbitals, the Kohn-Sham formalism was developed. The Kohn-Sham formalism provides a possibility to treat many-electron systems with a reasonable accuracy.[56;57] The ground state energy is within the Kohn-Sham formalism written as:

$$E[n] = T_s[n] + J[n] + V_{ext}[n] + E_{xc}[n] \tag{2.5}$$

$T_s[n]$ is the kinetic energy for a non-interacting reference system, $J[n]$ is the classical electron-electron repulsion energy, and $V_{ext}[n]$ is the nuclei-electron potential energy. The

exact solutions of these three classical terms are, in principle, available. However, the fourth term, which is the exchange-correlation energy ($E_{xc}[n]$) has no explicit exact form that can be solved exactly and will be discussed further in the subsection 2.3.2.

With the explicit form of the first three terms, the ground state electronic energy of a system can be written as:

$$E[n] = \sum_i \langle \phi_i | -\frac{1}{2}\nabla^2 | \phi_i \rangle + \frac{1}{2} \iint \frac{\rho(r)\,\rho(r')}{|r-r'|} dr\, dr' + \int \rho(r)\, v_{ext}(r) dr + E_{xc}[n] \quad (2.6)$$

Here ϕ_i is the set of one-electron Kohn-Sham orbitals and $\rho(r)$ is the electron density of the Kohn-Sham reference system, which is given by:

$$\rho(r) = \sum_i |\phi_i(r)|^2 \quad (2.7)$$

In the nuclei-electron potential energy term, $v_{ext}(r)$ is the external potential related to the nuclei and given by:

$$v_{ext}(r) = -\sum_{\alpha=1}^{n} \frac{Z_\alpha}{|\mathrm{r} - \mathrm{R}_\alpha|} \quad (2.8)$$

Where Z_α is the charge of the nuclei, and $|\mathrm{r} - \mathrm{R}_\alpha|$ is the distance between nuclei and a point in the electron density.

2.3.2   Approximations to the exchange-correlation functional

The exchange-correlation functional, which is the $E_{xc}[n]$ term in the Kohn-Sham formulation, is associated with the quantum mechanical effects of the electron-electron interactions.[57] $E_{xc}[n]$ can be regarded as the sum of an exchange term $E_x[n]$ and a correlation term $E_c[n]$:

$$E_{xc}[n] = E_x[n] + E_c[n] \quad (2.9)$$

The description of the $E_{xc}[n]$ term is the biggest challenge in DFT and the approximate nature of the exchange-correlation functional limits the accuracy of the method. The difference in accuracy between the various approximations is sometimes pictured through the famous Jacob's ladder of approximations,[57–59] as shown in Fig. 2.1.
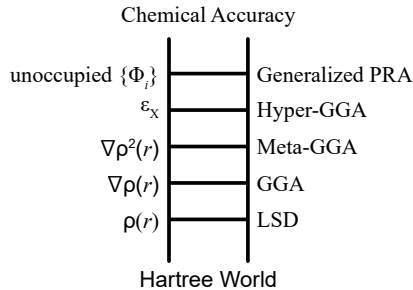

Figure 2.1: Jacob's ladder of density functional approximations, from Ref. 58.

In the Hartree world, the exchange-correlation functional is not included, and thus, it is not able to predict the properties of the system properly. With different approximations and attempts to introduce the nature of the exchange-correlation functional into DFT calculation, the ultimate goal is to reach chemical accuracy, which is defined as an accuracy of about 0.04 eV. Compared with local density approximation (LDA), DFT calculations that adopted generalized gradient approximation (GGA) or meta-GGA provide reasonable accuracy for many systems[60] with acceptable calculation costs and, therefore, have been widely used. However, GGA and meta-GGA still have the self-interaction error and the van der Waals interactions are not taken into account; thus, further improvements are needed to achieve higher accuracy. The common approximations are discussed below.

Local density approximation

The local density approximation (LDA) is the simplest approach to describe the exchange-correlation functional. It uses the expression of the uniform electron gas model[54] to represent the exchange energy ($E_x^{\mathrm{LDA}}[\rho]$) in terms of the electron density. The expression of the exchange energy was given by Dirac in 1930:[61]

$$E_x^{\mathrm{LDA,Dirac}}[\rho] = -\frac{3}{4}\left(\frac{3}{\pi}\right)^{\frac{1}{3}} \int \rho^{\frac{4}{3}}\, dr \qquad (2.10)$$

The correlation energy $E_c^{\mathrm{LDA}}[\rho]$ can for the uniform electron gas be obtained by exact quantum Monte Carlo simulation.[62] Such simulations have been parameterized to develop functionals for the correlation.[63]

Although the concept of LDA is relatively simple, this approximation is surprisingly good, especially for the simple metal systems that have close to homogeneous valence electron densities. The problem of LDA, however, is that it normally overestimates the ionization energies and bond strengths.[55;57] Moreover, systems with large gradients in the valence electron density will not be described accurately.

Generalized gradient approximation

To obtain an accurate description of molecular systems with an inhomogeneous electron density, better methods that, in addition to the density, also include the gradient of the density $[\nabla\rho]$ have been developed.[64] In the early work, the gradient expansion approximation (GEA) was introduced to provide a gradient correction to the standard exchange energy density in a situation with slowly varying density.[65] The gradient expansion is developed by the dimensionless reduced gradient, which is given by

$$s = \frac{|\nabla\rho|^{\frac{4}{3}}}{\rho} \qquad (2.11)$$

and the exchange energy from gradient expansion approximation can be represented as:[55]

$$E_x^{\mathrm{GEA}} = -\int \rho^{\frac{4}{3}}\left[\frac{3}{4}\left(\frac{3}{\pi}\right)^{\frac{1}{3}} + \frac{7}{432\pi(3\pi^2)^{\frac{1}{3}}}s^2 + ...\right] dr \qquad (2.12)$$

However, the GEA is reasonable only for systems with slowly varying electron densities.[55] For systems with exponentially decaying density ($s \rightarrow \infty$), GEA will not be able to give accurate results.[55] The development of generalized gradient approximation (GGA) addresses this problem by introducing the gradient expansion in the low s limit (represented as $F(s)$), where the energy is given by:[55]

$$E_x^{\text{GGA}}[\rho, s] = \int \rho^{\frac{4}{3}} F(s) dr \tag{2.13}$$

Many exchange functionals of the GGA type have been proposed, for example, B88, PW91, and PBE. The Perdew-Burke-Ernzerhof-GGA functional (PBE) was adopted in this thesis.[64] In recent years, meta-GGA methods that take the kinetic energy density $[\nabla^2 \rho]$ into account have been proposed and have been shown to provide higher accuracy.[66] For the correlation energy of GGA, E_c^{GGA}, it can be expressed by:

$$E_c^{\text{GGA}}[\rho] = \int d^3 r \rho [\epsilon_c^{\text{unif}}(r_s, \zeta) + H(r_s, \zeta, t)] \tag{2.14}$$

where r_s is the local Seitz radius, ζ is the relative spin polarization and t is a dimensionless density gradient.[64]

Hybrid GGA

One of the main sources of the inaccuracy of GGA calculations is the self-interaction error. It comes from the fact that the electron self-interaction in the classical Coulomb energy is not canceled by the corresponding interaction in the exchange part,[67;68] which is the case in the wavefunction-based Hartree-Fock theory. According to this property, hybrid functionals, which are the combination of the exchange-correlation functional from the GGA method and a certain amount of Hartree-Fock (HF) exchange were developed.[55;68]

The Heyd-Scuseria-Ernzerhof hybrid functional (HSE)[69] is one often used hybrid functional. In HSE, a spatial decay of the HF exchange interaction is accelerated by the substitution of the full $1/r$ Coulomb potential with a screened interaction. Here the Coulomb potential is split into short-range (SR) and long-range (LR) components and the the screening parameter ω is used to define the separation range. The exchange-correlation energy is in HSE calculated as:

$$E_{xc}^{\text{HSE}} = \alpha E_x^{\text{HF,SR}}(\omega) + (1 - \alpha) E_x^{\text{PBE,SR}}(\omega) + E_x^{\text{PBE,LR}}(\omega) + E_c^{\text{PBE}} \tag{2.15}$$

Here $E_x^{\text{HF,SR}}$ is the short-range HF exchange, $E_x^{\text{PBE,SR}}$ and $E_x^{\text{PBE,LR}}$ are the short- and long-range components of the PBE exchange functional from the integration of the model PBE exchange hole, and E^{PBE} is the correlation energy from PBE. Depending on the value of ω, there are the HSE03 and HSE06 versions of HSE. HSE provides better thermochemical results and good accuracy for lattice constants as well as band gaps in oxides and solids than pure PBE.[70] However, the computational cost of HSE is much higher than PBE. Calculating the energy of $[\text{Cu}_2(\text{NH}_3)_4\text{O}_2]^{2+}$ in the CHA cage, which is a system of 56 atoms, takes 21 hours with HSE and only 1 hour with PBE.

DFT+U

As mentioned, conventional LDA and GGA methods have difficulties in accurately describing systems with localized electrons due to the self-interaction error. To describe systems with localized electrons without the high computational cost as in HSE, an on-site Hubbard term can be introduced to eliminate the delocalization error. The definition of Hubbard parameter U is:[71]

$$U = E(d^{n+1}) + E(d^{n-1}) - 2E(d^n) \tag{2.16}$$

which defines the cost of Coulomb energy for putting two electrons at the same site. In this way, the self-interaction error can be partly eliminated. A comparative test between different density functionals[72] revealed that only a functional with the Hubbard-U term can correctly describe the experimental preference of Cu_2O_2 crystals. In my work, DFT+U is applied to describe the localized Cu(3d) electrons, which is especially important for the Cu-peroxo species.

It is worth noting that the parameters of Hubbard-U term (U and J) are generally extracted from ab-initio calculations or obtained by comparing with experimental measurements.[73] However, during reactions, especially redox reactions, the value of these parameters may change along the reaction path. Thus, solving the problem of over-delocalization by introducing the Hubbard-U term has limitations.

van der Waals interaction and exchange-correlation functionals

For unbound chemical species, long-range electronic correlations exist between the non-overlapping densities and these correlations are the so-called van der Waals (vdW) interactions. The vdW interactions are not included in pure DFT-based functionals[55] and leads to an inaccuracy in the description of sparse matter.

To take the vdW interaction into account, one approach is to develop a nonlocal exchange-correlation functionals, where the vdW interactions are treated in the same electron-(spin-)density framework as the other interactions. Based on this approach, Lundqvist *et al.*[74] proposed a non-empirical vdW-DF functional that included the long-range form of the interaction. Recently developed versions are the regular range-separated hybrid functionals, such as vdW-DFs, AHCX and AHBR. In this way, both the SIE and vdW interactions can be considered and expected to result in higher accuracy.[75;76]

An alternative semi-empirical approach to account for vdW interaction is to introduce an attractive $1/R^6$ behavior by including the empirical pairwise correction, which is the DFT-D method. Due to the acceptable accuracy with much lower computational cost than vdW-DF methods, the relatively new version of DFT-D method, DFT-D3,[77] is employed in this work.

2.3.3 Solution to the Kohn-Sham equations

DFT in the Kohn-Sham formulation is used in electronic structure calculations to simplify the Schrödinger equation from a many-body problem into one-particle Kohn-Sham equations. To bring DFT into practice, different approaches have been adopted to solve

the Kohn-Sham equations. One important choice is the method of expanding the wave-functions. In this work, the studied system are periodic, and thus, plane waves that have inherent periodicity are chosen to expand the Kohn-Sham orbitals.

Besides the way to expand the wavefunctions, one also needs to consider how to treat the core electrons. The projector augmented-wave (PAW) method proposed by Blöchl[78] in 1994 is a widely used method. In the PAW method, the all-electron (AE) wavefunctions, $|\Psi\rangle$, are transformed into computationally convenient pseudo (PS) wavefunctions, $|\tilde{\Psi}\rangle$. Here the AE wavefunctions are full one-electron Kohn-Sham wavefunctions, while the PS wavefunctions can be identified with the wavefunctions of the pseudopotential approach.[78] Through the transformation, the AE wavefunction can be described by the equation below from the PS wavefunction:

$$|\Psi\rangle = |\tilde{\Psi}\rangle + \sum_i (|\phi_i\rangle - |\tilde{\phi}_i\rangle)\langle\tilde{p}_i|\tilde{\Psi}\rangle \tag{2.17}$$

Here $|\phi_i\rangle$ is one of the AE partial waves, $|\tilde{\phi}_i\rangle$ is one PS partial wave, and $|\tilde{p}_i\rangle$ is the projector functional for each PS partial wave that localized with the augmentation region.

To obtain the ground state solution from the Kohn-Sham equations, a self-consistent field (SCF) loop is applied in the calculations. A schematic of the SCF loop is shown in Fig. 2.2.
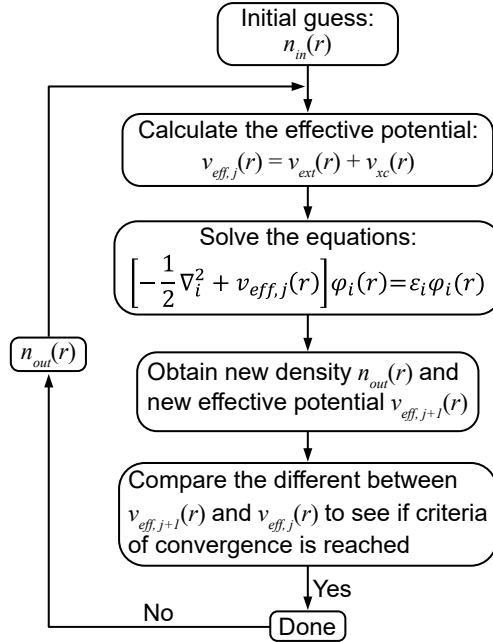

Figure 2.2: Schematic of self-consistent field loop to obtain the ground state. Adapted from Ref. 79, page 3-2.

The loop starts with an initial guess of the plane-wave weights and electron density.

The Kohn-Sham equations are solved by calculating the effective potential. A new electron density and effective potential will be obtained. After solving the equation, the energy difference between the latest effective potential ($v_{eff,j+1}$) and the effective potential from the previous loop ($v_{eff,j}$) will be compared until the latest solution reaches the criteria of convergence.

In this thesis, the Vienna *ab initio* simulation package (VASP)[80;81] that uses a plane-wave basis set and the PAW method is applied.

Chapter 3

Calculations of measurable properties

The previous chapter introduced the approximations and methods in DFT, which provide a basis for electronic structure calculations making it possible to calculate the total electronic energy and electronic structure for the systems of interest. The development of DFT has greatly advanced the practical use of calculations in materials science. It offers the possibility of predicting geometrical structures, calculating various physical properties, and simulating reaction processes that involve electronic hybridization, which facilitates the integration of theoretical calculations and experimental measurements. The calculations of measurable properties are discussed in this chapter.

3.1   Geometry optimization

Calculation of the electronic structure as well as the corresponding total energy is possible for a collection of atoms in an arbitrary structure. By comparing the energy of the system with the same atoms but different atomic arrangements, the structure that has the lowest energy can be found. The structure with the lowest energy has the highest stability and, thus, the most probable structure to observe. This operation of finding the most stable structure is the so-called, geometry optimization. Various methods have been developed to obtain efficient optimization techniques.[82]

The local quadratic approximation of the potential energy surface can be constructed by the first and second derivatives of the energy with respect to geometrical parameters:

$$E(\mathrm{x}) = E(\mathrm{x_0}) + \mathrm{g}_0^T \Delta \mathrm{x} + \frac{1}{2}\Delta \mathrm{x}^T \mathrm{H_0} \Delta \mathrm{x} \qquad (3.1)$$

Here, the gradient $(\mathrm{d}E/\mathrm{dx})$ at $\mathrm{x_0}$ is represented by the transpose of $\mathrm{g_0}$, the Hessian $(\mathrm{d}^2 E/\mathrm{dx}^2)$ at $\mathrm{x_0}$ is given by the $\mathrm{H_0}$ and $\Delta \mathrm{x} = \mathrm{x\text{-}x_0}$. By probing the potential energy surface, it is possible to obtain a minimum energy as well as the corresponding structure. The techniques used for geometry optimization are presently mainly dependent on the first derivative of the energy. Currently, the major methods for optimizing geometries are the Newton method, quasi-Newton methods, and the conjugate gradient methods.[83] In VASP, the conjugate-gradient method[84] was implemented to find the optimized structure and evaluate the minimum total energy.

The work in this thesis is focused on the NH_3-SCR reaction over Cu-CHA. The cage structure of CHA and the high mobility of different Cu-complexes lead to a flat potential energy surface, which makes it difficult to find the global minimum. To obtain the low-energy configurations, *ab initio* molecular dynamics simulation was adopted as an additional tool to probe the potential energy surface.

The concept of *ab initio* molecular dynamics (AIMD)[85] is that the motion of the atoms can calculated by solving the Newton's laws of motion ($F = ma$) with a force obtained by DFT. The most common algorithm to integrate AIMD equations is the Verlet algorithm,[86] which can enable the calculation of motion trajectories with acceptable accuracy and computational cost.

AIMD can be performed to simulate the motion of the system at a set temperature, which results in the atomic trajectory and the corresponding energy. In this way, MD calculations can be used to search for low-energy configurations for systems with a flat potential energy surface. Here, Born-Oppenheimer MD was used, which enforces explicitly the minimum condition for the electrons at each update of the nuclear coordinates, and the simulations were performed within the canonical ensemble. Accordingly, the movement of the molecules at a certain temperature can be simulated and the corresponding energies can be calculated. By selecting a relatively stable configuration within the AIMD simulation and performing geometry optimization, the most stable structure can be found and avoiding the situation where only local minimum can be found, as shown in Fig. 3.1. Also, scanning the potential energy surface with AIMD can help to obtain the time-averaged properties of the system at a certain temperature.
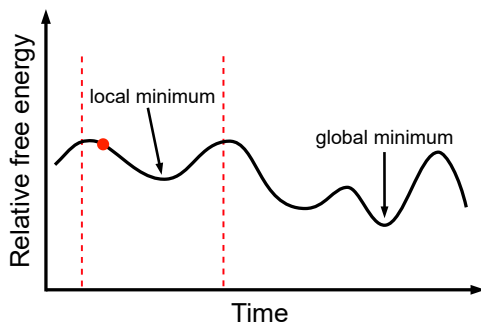

Figure 3.1: Schematic of the difference between finding the most stable structure by geometry optimization and geometry optimization with AIMD. Starting with the red point, geometry optimization only would result in the indicated local minimum. AIMD in combination with geometry optimization can obtain the global minimum.

3.2 Vibrational frequency analysis and simulated infrared spectra

Vibrational spectra is of great importance in chemical research because it helps the elucidation of the reaction mechanisms and structure of the adsorbed species by giving the vibrational modes of chemical bonds. For common molecules, the structures can be inferred by comparing them to the specific wavenumber of known vibrational modes. For more complex situations, since the vibrational frequencies of the different bonds in the molecule can also be obtained by DFT calculations, the suggested structure of an unknown molecule can be determined by comparing the measured vibrational frequencies

with the simulated vibrational frequencies of a guessed molecule or configuration. [87] (p. 130) By combining with Density-Functional Perturbation Theory, vibrational analysis with intensity information can be obtained in VASP. [88] Simulated vibrational spectra can provide a more direct comparison with experimental measurements to analyze complex adsorption systems. Fig. 3.2 shows the simulated vibrational spectra of NH_3^+ on H-CHA, where the wavenumber and intensity of each frequency are given.
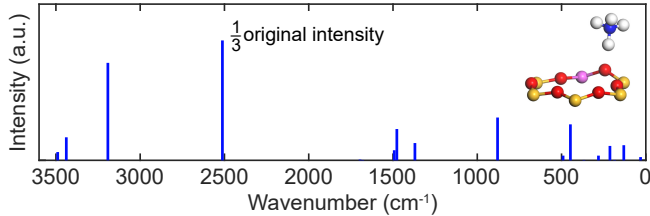

Figure 3.2: Simulated vibrational spectra of NH_3^+ on H-CHA. The vibrational frequency near 2500 cm^{-1} has a particularly high intensity. To make other frequencies with low intense visible, the figure multiplies the peak near 2500 by one-third.

The calculated vibration frequencies are also used in the zero-point correction of the electronic energies. General DFT calculations are performed at a temperature of 0 K and the obtained total electronic energy ($E_{\mathrm{non-ZPE}}$) does not include the zero-point energy that comes from the vibrational motion of the molecular system at 0 K.

The vibrations of a molecule can be seen as displacements of the atoms from the equilibrium structure. It is possible to expand the energy of the molecule around the equilibrium bond length by a Taylor expansion. The harmonic approximation neglects the higher-order terms in the Taylor expansion and the vibrational frequency can be obtained by combining Newton's and Hooke's laws. [89] For a system that has N atoms, there will be $3N$ degree of freedom and the Taylor expansion of the zero point energy (E_{ZPE}) for the atoms in the local minimum (x = 0) can be expressed as:

$$E_{\mathrm{ZPE}} = \frac{1}{2} \sum_{i=1}^{3N} \sum_{j=1}^{3N} \left[\frac{\partial^2 E}{\partial \mathrm{x}_i \partial \mathrm{x}_j} \right]_{\mathrm{x}=0} \Delta \mathrm{x}_i \Delta \mathrm{x}_j \tag{3.2}$$

where $\Delta \mathrm{x}_i$ and $\Delta \mathrm{x}_j$ are the displacements and a $3N \times 3N$ matrix, which is the so-called Hessian matrix, is defined by the derivatives. Following that, the normal modes are given by the $3N$ eigenvalues of the matrix. It should be noted that non-linear molecules have $3N$-6 vibrations, while linear molecules have $3N$-5 vibrations. The removed frequencies included 3 translations and 3 (or 2) rotations. For the system with i vibrational frequencies, the zero-point correction (E_{ZPE}) is given by:

$$E_{\mathrm{ZPE}} = \sum_i \frac{h \cdot v_i}{2} \tag{3.3}$$

where v_i is the vibrational frequencies (s^{-1}) and h is the Planck constant. Following that,

the zero-point corrected energy is:

$$E = E_{\text{non}-\text{ZPE}} + E_{\text{ZPE}} \tag{3.4}$$

In addition, the calculated frequencies can be used to confirm local minima and transition state structures, as well as to evaluate the vibrational entropy, which will be further discussed in Section 3.3 and Chapter 3.5.

3.3 Energy barriers

Based on experimental observations, Arrhenius proposed an empirical expression for the rate constant of a catalytic reaction:

$$k = A e^{-\frac{E_{app}}{k_{\text{B}}T}} \tag{3.5}$$

Here, k is the reaction rate constant at the absolute temperature (T), A is the pre-exponential factor, k_{B} is Boltzmann's constant, and E_{app} is the apparent activation energy. The role of the catalyst is to stabilize the transition state to reduce E_{app} and, thus, facilitate the reaction.

The concept of activation energy is used in the Arrhenius equation and also in transition state theory (TST).[15 (p. 107-109)] The TST provides a thermodynamic formulation of the Arrhenius equation by assuming that the reactants (R) are activated to the transition state ($R^{\ddagger}$) in order to form the product (P).[15 (p. 108)] $R^{\ddagger}$ is the configuration that has the highest energy along the reaction coordinate. A schematic of the transition state is shown in Fig. 3.3 and the energy difference ($\Delta E^{\ddagger}$) between $R^{\ddagger}$ and R is the activation energy of the reaction.
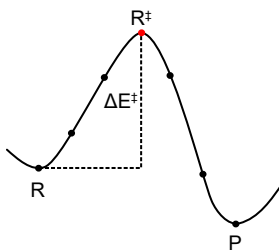

Figure 3.3: Schematic of the barrier connecting the reactants (R) with the products (P) via the activated complexes ($R^{\ddagger}$). $\Delta E^{\ddagger}$ is the energy difference between $R^{\ddagger}$ and R.

Following the assumptions in TST, a reaction can be described by the reaction coordinate that links the reactant (initial state), transition state, and product (final state). The rate of a forward reaction from reactant to the transition can be evaluated by the partition functions of the initial state (Z) and the transition state without the reaction coordinate ($Z^{\ddagger}$), assuming equilibrium between the initial and transition state. The expression of rate constant within TST is:

$$k^{\text{TST}} = \frac{k_{\text{B}}T}{h} \frac{Z^{\ddagger}}{Z} \tag{3.6}$$

For the backward reaction, Z is the partition function of the final state. Using the thermodynamic formulation, the TST rate constant is:[90 (p. 109)]

$$k^{\text{TST}} = \frac{k_{\text{B}}T}{h}e^{-\Delta G^{\ddagger}/k_{\text{B}}T} = \frac{k_{\text{B}}T}{h}e^{\Delta S^{\ddagger}/k_{\text{B}}}e^{-\Delta H^{\ddagger}/k_{\text{B}}T} \approx \frac{k_{\text{B}}T}{h}e^{\Delta S^{\ddagger}/k_{\text{B}}}e^{-\Delta E^{\ddagger}/k_{\text{B}}T} \qquad (3.7)$$

Where $\Delta G^{\ddagger}$ is the difference in Gibbs free energy between the initial and transition states. $\Delta S^{\ddagger}$ and $\Delta H^{\ddagger}$ are the corresponding differences in entropy and enthalpy, respectively. The pV-dependence in the enthalpy is neglected, so the change in enthalpy becomes equal to the change in energy ($\Delta E^{\ddagger}$).

To obtain $\Delta S^{\ddagger}$ and $\Delta H^{\ddagger}$, it is necessary to find the minimum energy path by probing the energy paths between the initial and final state. The top of the minimum energy path is the transition state, which is also a saddle point of the potential surface. It should be noted that the saddle point is the local maxima along the reaction direction but the local minimum in all other directions. Vibrational frequency calculation is performed on the suggested transition state to confirm it has a first-order saddle point. A transition state should only have one imaginary vibrational frequency. Different methods have been developed for minimum energy path probing, and the nudged elastic band (NEB) method is an efficient method that is widely used.[91]

The NEB method works by constructing a number of images between the initial and final state. Spring forces are added along the band between images to ensure the continuity of the path, which is why the method is called elastic band. When finding the lowest energy possible for each image, the tangent to the path will be estimated at every iteration in order to decompose the true force and the spring force. Only the perpendicular component of the true force and the parallel component of the spring force are included during the minimization.[91] With modifications to the NEB method, the climbing image NEB was developed providing a more precise estimation of the saddle point.[92]

With the transition state from NEB simulations, the rate constant can be calculated by eq.(3.7), which can further be used in kinetic modeling and deriving other experimentally measurable kinetic parameters. In this way, theoretical calculations allow for a more direct comparison with experimental measurements, resulting in an improved understanding of the reaction mechanism.

3.4 Atomic charges

The catalysis of redox reactions relies on charge transfer. Charge analysis is one powerful tool to study the state of the active sites during the reaction paths. Bader charge analysis[93] is a useful method to evaluate the distribution of the electron density, which can also provide information on change transfer. The principle of charge analysis is to split the density of the molecule into contributions from each atom. Bader suggested that the space in the systems can be divided by the charge density and the divided space is called Bader volumes. The difficulty in Bader analysis is the calculation of Bader volumes. The grid-based Bader algorithm developed by Henkelman and coworkers[94] used the path along the steepest descent to define the Bader volumes where the charge is localized. The Bader analysis algorithm was applied in the present work.

3.5 Evaluation of entropy

Accurate estimations of entropy and enthalpy changes are important to obtain rate constants that describe the reaction kinetics. The NH_3-SCR reaction occurs over Cu-CHA, which is a catalyst that is more complex than a typical solid surface. There are two main types of adsorption sites of NH_3 in Cu-CHA, namely the Brønsted acid site and the Cu-site. When NH_3 is adsorbed on the Brønsted acid site, it will form NH_4^+, which is not directly bonded to the framework. However, the motion is significantly restricted. For the adsorption on the Cu-site, Cu^+ can adsorb up to four NH_3 and form $[Cu(NH_3)_n]^+$ (n = 1 - 4). In the absence of ligands such as NH_3, Cu is bound to the CHA framework, and preferentially located in the six-membered ring in the CHA. When the first NH_3 is adsorbed on Cu^+, the Cu cation is pulled up but still bound to the CHA framework. Once $[Cu(NH_3)_{n \geq 2}]^+$ is formed, the complex will detach from the framework and become a mobile species. The optimized structures of the CHA framework, H-CHA, NH_3 in H-CHA, and $[Cu(NH_3)_n]^+$ (n = 1 - 4) from DFT calculation are shown in Fig. 3.4. The mobility of NH_3-solvated Cu-complexes has been verified by X-ray absorption spectroscopy measurements.[95;96]
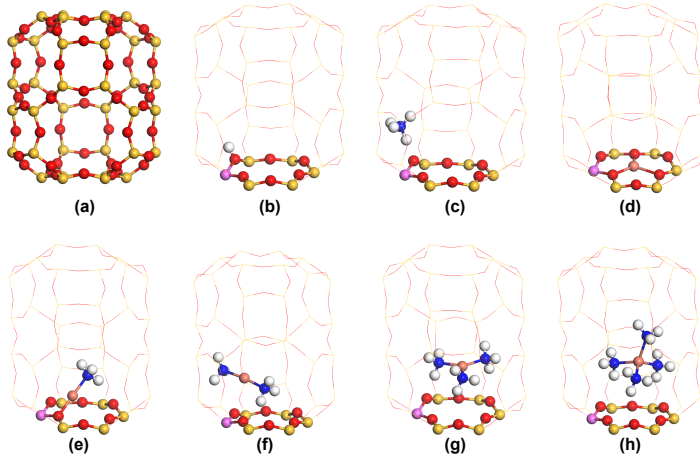

Figure 3.4: Structures of CHA models. (a) Al-free CHA, (b) H-CHA, (c) NH_3 on Brønsted acid site (forming NH_4^+) (d) Cu cation on Al-CHA, and (e - h) $[Cu(NH_3)_n]^+$ (n = 1 - 4) in CHA. Atomic color codes: H (white), N (blue), O (red), Si (yellow), Al (pink) and Cu (bronze).

Based on statistical mechanics and thermodynamics,[97] the entropy (S) can be calculated from the partition function (Z):

$$S = -\frac{\partial}{\partial T}(-k_B T \ln Z)_{V,N} = k_B \ln Z + k_B T \frac{1}{Z}\left(\frac{\partial Z}{\partial T}\right)_{V,N} \tag{3.8}$$

Z is the product of the partition functions corresponding to translations, rotations, and vibrations. The main contribution to the entropy originates from translations and the

partition function of translations is sensitive to how translations are handled. To have an accurate evaluation of the entropy of different Cu complexes in Cu-CHA, different methods have been adopted according to the differences in mobility. This section elaborates on the methods used to evaluate the entropy and shows the validity by comparisons to NH$_3$-temperature programmed desorption (NH$_3$-TPD) experiments.

3.5.1 Entropy for gas-phase molecules

A gas-phase molecule is a free translator confined by pressure in three-dimensional space. The volume of this space is given by the pressure through the ideal gas law for one molecule ($pV = k_\mathrm{B}T$). In this case, the total partition function and the total entropy is respectively (putting the electronic and nuclear partition functions to 1):[90 (p. 87-91)]

$$Z^{\mathrm{gas}} = Z^{\mathrm{gas}}_{\mathrm{rot}} Z^{\mathrm{gas}}_{\mathrm{vib}} Z^{\mathrm{gas}}_{\mathrm{trans}} \tag{3.9}$$

$$S^{\mathrm{gas}} = S^{\mathrm{gas}}_{\mathrm{vib}} + S^{\mathrm{gas}}_{\mathrm{rot}} + S^{\mathrm{gas}}_{\mathrm{trans}} \tag{3.10}$$

Here, $S^{\mathrm{gas}}_{\mathrm{vib}}$, $S^{\mathrm{gas}}_{\mathrm{rot}}$, and $S^{\mathrm{gas}}_{\mathrm{trans}}$ are the vibrational, rotational, and translational entropies, respectively.

Contributions from translations

The translational partition function for a gas-phase molecule is:[90 (p. 86)]

$$Z^{\mathrm{gas}}_{\mathrm{trans}} = \left(\frac{2\pi m k_B T}{h^2}\right)^{\frac{3}{2}} V \tag{3.11}$$

where m is the mass of the molecule and the volume V is obtained by the pressure and temperature. Following eq. (3.8), the translational entropy per molecule in a gas is:[98]

$$S^{\mathrm{gas}}_{\mathrm{tran}} = k_\mathrm{B}\left[\ln(Z^{\mathrm{gas}}_{\mathrm{trans}}e) + T\left(\frac{3}{2T}\right)\right] = k_\mathrm{B}\left[\ln Z^{\mathrm{gas}}_{\mathrm{trans}} + \frac{5}{2}\right] \tag{3.12}$$

Contributions from rotations

The rotational partition function of a molecule depends on the structure and have different expressions for linear and non-linear molecules:

$$Z^{\mathrm{gas}}_{\mathrm{rot_{linear}}} = \frac{1}{\sigma}\left(\frac{8\pi^2 I k_B T}{h^2}\right) \tag{3.13}$$

$$Z^{\mathrm{gas}}_{\mathrm{rot_{non-linear}}} = \frac{\sqrt{\pi}}{\sigma}\left(\frac{8\pi^2 k_B T}{h^2}\right)^{\frac{3}{2}} \sqrt{I_x I_y I_z} \tag{3.14}$$

Here σ is the symmetry factor of molecule and I_i are the moments of inertia. The I_i values used in this thesis were obtained through the Atomic Simulation Environment (ASE).[99;100] The partial derivative term of Z_{rot} in eq. (3.8) is equal to $3/2T$ for non-linear molecule while it is $1/T$ in linear molecule. Thus, the equations of rotational entropy per linear and non-linear molecule are:

$$S^{\mathrm{gas}}_{\mathrm{rot_{linear}}} = k_\mathrm{B}(\ln Z^{\mathrm{gas}}_{\mathrm{rot_{linear}}} + 1) \tag{3.15}$$

$$S^{\mathrm{gas}}_{\mathrm{rot_{non-linear}}} = k_\mathrm{B}(\ln Z^{\mathrm{gas}}_{\mathrm{rot_{non-linear}}} + \frac{3}{2}) \tag{3.16}$$

Contributions from vibrations

As mentioned in section 3.2, the number of vibrational modes is $3N$-6 for non-linear molecules, while it is $3N$-5 for linear molecules where N is the number of atoms in the molecule. Based on the harmonic approximation at constant volume,[90 (p. 90)] the vibrational entropy can be described by the harmonic vibrational frequencies:

$$
\begin{aligned}
S^{\text{gas}}_{\text{vib}} &= k_{\text{B}} \left[\ln(Z^{\text{gas}}_{\text{vib}} e) + T \left(\frac{\partial \ln Z^{\text{gas}}_{\text{vib}}}{\partial T} \right)_V \right] \\
&= k_{\text{B}} \sum_m \left[\frac{\Theta_{v,m}/T}{e^{\Theta_{v,m}/T} - 1} - \ln(1 - e^{-\Theta_{v,m}/T}) \right]
\end{aligned}
\tag{3.17}
$$

Here, m is the index of the vibration modes is m. Working with zero-point corrected energies, the expression of the vibrational entropy takes the form:[98]

$$
\begin{aligned}
S^{\text{gas}}_{\text{vib}} &= k_{\text{B}} \left[\ln(Z^{\text{gas}}_{\text{vib}} e) + T \left(\frac{\partial \ln Z^{\text{gas}}_{\text{vib}}}{\partial T} \right)_V \right] \\
&= R \sum_m \left[\frac{1}{(1 - e^{-\Theta_{v,m}/T})} \right]
\end{aligned}
\tag{3.18}
$$

Here Θ is the vibrational temperature, which is defined as:

$$
\Theta_{v,m} = \frac{h v_m}{k_B}
\tag{3.19}
$$

where v_m is the vibrational frequency for mode m.

3.5.2 Entropy for adsorbates

In the cases that a molecule is chemically bound to a surface, it is often assumed that the molecule will lose all rotation and translation. Thus, the entropy of adsorbates on a surface can be calculated with the vibrational modes with the harmonic approximation, i.e., treating translations and rotations as frustrated vibrations. In the CHA system, the adsorbates have different adsorption properties, and different methods were therefore used to evaluate the entropy.

For the entropy of framework-Cu species (structure (d) in Fig. 3.4), a refinement with respect to the harmonic approximation was used, namely the complete potential energy sampling (CPES) method.[101] In this approach, the translational partition function is estimated by explicit calculations of the potential energy of the adsorbates. This semiclassical canonical partition function is given by:

$$
Z^{\text{CPES}}_{\text{trans}} = \frac{2\pi m k_{\text{B}} T}{h^2} \iint exp \left(\frac{-V(x,y)}{k_{\text{B}} T} \right) dx\, dy
\tag{3.20}
$$

The integration is performed numerically over the surface cell, and $V(x,y)$ is the potential energy as a function of position (x,y) as obtained by DFT calculations. The potential energy $V(x,y)$ is obtained by interpolating between a set of calculated points in the

surface cell. In this thesis, the complete potential energy sampling of Cu cation adsorbed on the six-membered ring of CHA is performed, and the potential energy landscape is given in Fig. (3.5). The comparison between the entropy of framework Cu from harmonic approximation and CPES method shows that the harmonic approximation results in an overestimation of the entropy by $\sim$10 J/K in the investigated temperature range (200 - 900K).
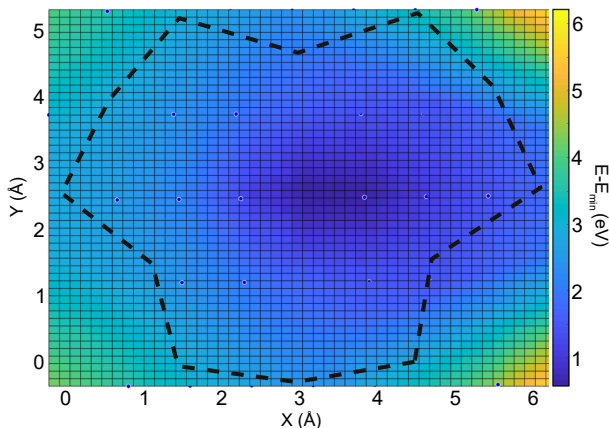

Figure 3.5: Potential energy landscape for Cu on the six-membered ring of CHA. The energies are given with respect to minimum for Cu. The black dashed line represents the six-membered ring of CHA and the blue dots are the sampling points.

For $[Cu(NH_3)]^+$, where one NH_3 ligand is bound to the CHA framework through a Cu cation, a part of translations and rotations on the complex are maintained according to the single bond between Cu and the framework. Thus, a standard harmonic approximation would underestimate its entropy by treating it as a surface adsorbed NH_3. In this work, the entropy of $[Cu(NH_3)]^+$ is evaluated as the vibrational entropy of the entire Cu-NH_3 complex.

3.5.3   Entropy for mobile species in CHA

In the CHA cage, molecules can move freely to a certain extent but are restricted compared to molecules in the gas phase. One suggested approach is to treat them as adsorbates but with free translator methods[101], where all the remaining degrees of freedom are treated as vibrations. However, this method often underestimates the molecular entropy for species in zeolites as they are weakly bounded and still maintain a part of translations and rotations.

By comparing with the CPES simulation mentioned in 3.5.2, it was found that non-bound small molecules in zeolites retain about 2/3 of their translational and rotational entropy from gas-phase.[40;102] Following that, the entropy of the mobile species in the

zeolite, S^{zeo}, is:

$$S^{\text{zeo}} = S_{\text{vib}}^{\text{zeo}} + \gamma \left(S_{\text{rot}}^{\text{gas}} + S_{\text{trans}}^{\text{gas}} \right) \tag{3.21}$$

where $S_{\text{vib}}^{\text{zeo}}$ is the vibrational entropy calculated in the zeolite. γ is an effective scaling coefficient, which was set to 2/3 for non-bound small molecules in zeolites. However, the bulky molecules or highly restricted molecules, for example $[\text{Cu(NH}_3)_{n\geq2}]^+$ and NH_3 on Brønsted acid sites in CHA, are likely to be even more hindered by the zeolite structure.

3.5.4 NH$_3$-temperature programmed desorption simulations

One way to verify the entropy calculations is to compare the results with temperature-programmed desorption (TPD) experiments. In this thesis, NH$_3$-TPD, which is widely used to determine the adsorption strength and storage capacity of NH$_3$ in zeolite experimentally, was introduced for this purpose. Following the method proposed in previous works, [103;104] we simulated NH$_3$-TPD profiles with the entropy and enthalpy differences in the NH$_3$ desorption process. In this section, the method of simulation and the way we determined the effective scaling coefficient γ in eq. (3.21) will be presented.

Evaluation of NH$_3$-TPD

The simulation of NH$_3$-TPD is based on the equilibrium between the gas-phase NH$_3$ and the adsorbed NH$_3$:

$$\text{NH}_3^* \underset{k_a}{\overset{k_d}{\rightleftharpoons}} \text{NH}_3(\text{g}) + * \tag{3.22}$$

here * is the adsorption site and NH$_3$(g) is the gas-phase ammonia. The adsorption and desorption rate constants are denoted by k_a and k_b, respectively. Taking the re-adsorption into account, the corresponding rate equation is:

$$\frac{d\theta}{dt} = k_a \frac{p_{\text{g}}}{p^0}(1 - \theta) - k_d \theta \tag{3.23}$$

Here θ is the NH$_3$ coverage, p_{g} is the pressure of NH$_3$, and p^0 is the standard atmospheric pressure. Combining the ideal gas law ($pV = k_{\text{B}}T$) with eq. (3.23), the concentration of NH$_3$, C$_{\text{g}}$, can be expressed as:

$$C_{\text{g}} = \frac{\theta}{1 - \theta} \frac{p^0}{k_{\text{B}}T} K \tag{3.24}$$

Where K is the equilibrium constant that can be evaluated by the enthalpy and entropy changes (ΔH and ΔS):

$$K = \frac{k_a}{k_b} = \exp\left(-\frac{\Delta H}{k_{\text{B}}T}\right) \exp\left(\frac{\Delta S}{k_{\text{B}}}\right) \approx \exp\left(-\frac{\Delta E}{k_{\text{B}}T}\right) \exp\left(\frac{\Delta S}{k_{\text{B}}}\right) \tag{3.25}$$

In this thesis, the ΔH is approximated as the zero-point corrected differential desorption energy of NH$_3$ from the different adsorption sites in Cu-CHA. The change in entropy (ΔS) is the difference in entropy before and after desorption.

In the TPD experiments, the amount of NH$_3$ that enter and exit from the catalyst can be measured and the mass balance is given by:

$$FC_{\mathrm{g}} = -A_0 W \frac{d\theta}{dt} \tag{3.26}$$

where F, A_0, and W are the flow rate of the carrier gas, the number of sites per weight catalyst, and the weight of the catalyst, respectively. Owing to the linear increase of temperature in the TPD, the relation between the change in time and temperature is $dT = \beta dt$. β is the heating rate. In this way, the expression of C_{g} is:

$$C_{\mathrm{g}} = -\frac{\beta A_0 W}{F} \frac{d\theta}{dt} = \frac{\theta}{1-\theta} \frac{p^0}{k_{\mathrm{B}} T} \exp\left(-\frac{\Delta E}{k_{\mathrm{B}} T}\right) \exp\left(\frac{\Delta S}{k_{\mathrm{B}}}\right) \tag{3.27}$$

The concentration as a function of temperature is solved numerically by stepping the coverage:

$$\theta_{i+1} = \theta_i + \left(\frac{d\theta}{dT}\right)_i \Delta T \tag{3.28}$$

By plotting C$_\mathrm{g}$ versus temperatures, the simulated NH$_3$-TPD can be obtained and directly compared with the experimental NH$_3$-TPD for further analysis.

Determination of entropy by fitting to experimental NH$_3$-TPD

In the NH$_3$-TPD simulation, ΔE of each desorption step is calculated by DFT including the zero-point correction, while the ΔS is evaluated by the methods introduced above with eq. (3.21). To obtain the values of γ, we used the experimental NH$_3$-TPD as references.

As a first step, we targeted the NH$_3$-TPD for H-CHA, which is widely used to evaluate the storage capacity of NH$_3$ at Brønsted acid sites. With the proton on Brønsted acid sites, the adsorbed NH$_3$ is in the form of NH$_4^+$, which has a restricted translation but still maintains rotation and vibration as a gas phase species. Therefore, NH$_4^+$ entropy can be evaluated following eq. (3.21).

In the first attempt, the γ value was set to 2/3 according to the previous studies,[40;102] and the comparison between experiment and simulation curves is shown in Fig. 3.6(a). In this case, there is a clear difference between the experimental and simulated curves where the simulated desorption peak appears at higher temperatures. This result indicated that the entropy of NH$_4^+$ is overestimated. By reducing the γ value, the desorption peak shifts to a lower temperature and agrees well with the experimental NH$_3$-TPD when γ is set to 0.29, which is shown in Fig. 3.6(b and c).

Owing to the difference in the mobility between complexes, the simulation of the NH$_3$-TPD from the Cu$^+$ site is more complicated. In the evaluation of entropy, the framework-bound Cu$^+$ is calculated by the CPES method. [Cu(NH$_3$)]$^+$ is evaluated by the harmonic approximation. The rest of the complexes are calculated following eq. (3.21). A similar fitting process as in NH$_3$-TPD of Brønsted acid sites was performed to obtain a γ value. It is interesting to note that when γ is set to 0.29 in the entropy evaluation of [Cu(NH$_3$)$_2$]$^+$, agrees with the experimental NH$_3$-TPD as shown in Fig. 3.6(d).
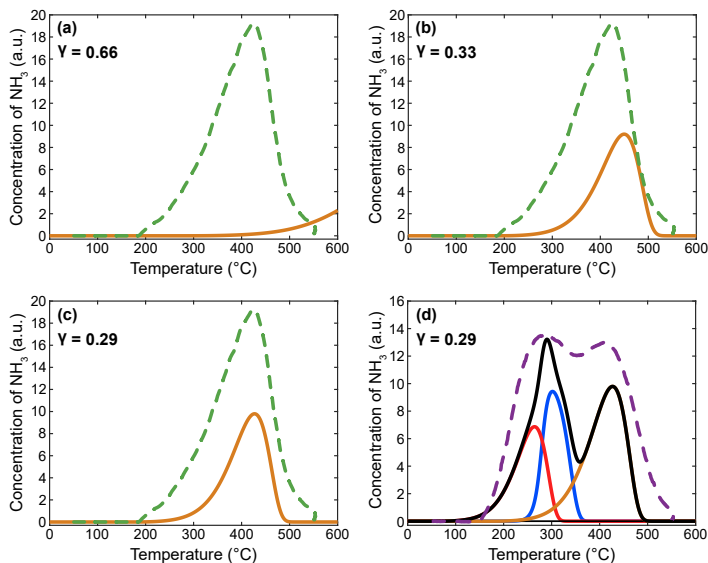
Figure 3.6: Simulated and experimental NH$_3$ desorption profiles in H-CHA(a, b and c) and Cu-CHA(d). The experimental profiles (green dashed line and purple dashed lines) are measured after NH$_3$ adsorption at 70 °C. The simulated profiles contains the NH$_3$ desorption from Brønsted acid site (orange lines), [Cu(NH$_3$)]$^+$ (blue line), [Cu(NH$_3$)$_2$]$^+$ (red line), and the sum of NH$_3$ desorption from each sites(black line). The experiment data is provided by Ton V.W. Janssens, Umicore.

3.5.5 Entropy change for O$_2$ adsorption over Cu-CHA

Oxygen adsorption over a pair of [Cu(NH$_3$)$_2$]$^+$ complexes is a key step in NH$_3$-SCR.[47] Through the adsorption process, a [Cu$_2$(NH$_3$)$_4$O$_2$]$^{2+}$ complex as shown in Fig. 3.7 is formed and Cu^I is oxidized into Cu^{II}. It is worth noting that as the complexes before
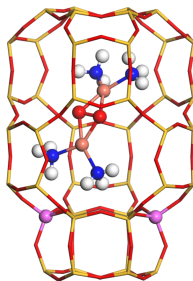

Figure 3.7: Side view of the chabazite cages showing the Al positions in the six-membered ring. The large cage includes the [Cu$_2$(NH$_3$)$_4$(O$_2$)]$^{2+}$ complex. Atomic color codes: H (white), N (blue), O(red), Si (yellow), Al (pink) and Cu (bronze).

and after the adsorption are relatively mobile, the entropy change during this process is difficult to estimate by conventional methods. In this thesis, we used the γ value from 3.5.4 to evaluated the entropies of $[Cu(NH_3)_2]^+$ and $[Cu_2(NH_3)_4O_2]^{2+}$ complex. Furthermore, the entropy differences of O_2 adsorption in the forward (ΔS_f^{zeo}) and backward reaction (ΔS_b^{zeo}) can be evaluated by:

$$\Delta S_f^{\text{zeo}} = S_{\text{TS},[Cu_2(NH_3)_4O_2]^{2+}}^{\text{zeo}} - (2\,S_{[Cu(NH_3)_2]^+}^{\text{zeo}} + S_{O_2}^{\text{gas}}) \tag{3.29}$$

$$\Delta S_b^{\text{zeo}} = S_{\text{TS},[Cu_2(NH_3)_4O_2]^{2+}}^{\text{zeo}} - S_{[Cu_2(NH_3)_4O_2]^{2+}}^{\text{zeo}} \tag{3.30}$$

Here $S_{\text{TS},[Cu_2(NH_3)_4O_2]^{2+}}^{\text{zeo}}$ and $S_{[Cu_2(NH_3)_4O_2]^{2+}}^{\text{zeo}}$ are the entropies of the transition and final state configurations of the adsorption, respectively. $S_{[Cu(NH_3)_2]^+}^{\text{zeo}}$ is the entropy of one $[Cu(NH_3)_2]^+$ complex in the zeolite.

In the recent experimental work of the O_2 adsorption on a pair of $[Cu(NH_3)_2]^+$ complexes, the entropy loss was measured to be 142 J/mol $\cdot$ K.[105] With the method proposed above, our computational entropy difference is 152 J/mol $\cdot$ K, which shows a good agreement with the measured entropy change. The successful evaluation of entropy loss from first principles calculation further validates the γ value obtained by fitting with experimental NH_3-TPD.

Chapter 4

Microkinetic modeling

With DFT calculations, we can obtain the reaction energy and barrier of elementary reactions to further hypothesize the proper reaction mechanism. However, this is not sufficient to provide a full picture of the reaction. To obtain a more general understanding of the reactions and to compare them with experimental measurements, first principles-based reaction kinetic simulations are required. Kinetic simulation can give detailed insights that are difficult to obtain from experiments alone. In this chapter, the principles and applications of mean-field microkinetic modeling and kinetic Monte Carlo simulations that are used to investigate the kinetics of NH_3-SCR in my work will be presented.

4.1 Mean-field kinetic modeling

The basic approximations in mean-field microkinetic models are that the sample is large and uniform, and the adsorbates are randomly distributed. Moreover, the interaction between adsorbates is negligible.[90 (p. 52)] The equilibrium reaction rate and coverages are in the mean-field approach achieved by the numerical solutions of a set of coupled ordinary differential equations. The differential equation that describes the time evolution of the adsorbate coverages of species i can be written as:

$$\frac{d\theta_i}{dt} = \sum_j r_j(\overrightarrow{\theta})c_{ij} \qquad (4.1)$$

Here θ_i is the fractional coverage of species i and the rate of reaction j is given by r_j. r_j depends on the fractional coverages ($\overrightarrow{\theta}$). c_{ij} is the number of i-molecules consumed in reaction j. In this work, the ode23s solver within MATLAB was adopted to integrate the system of differential equations numerically until steady-state is reached. According to eq. (3.6) and eq. (3.7), the rate constant of each elementary step can be calculated by their respective changes in energy and entropy. For each elementary step, the net rate can be written as:

$$r_j = k_j^+ \prod_f \theta_f - k_j^- \prod_b \theta_b \qquad (4.2)$$

Here f is the reactant species that participates in the forward reaction of elementary step j, while b represented the backward reaction.

4.2 Kinetic Monte Carlo simulations

An alternative method to solve the kinetic equations is the kinetic Monte Carlo (kMC) approach. The adsorbate distribution is treated explicitly in kMC and the method allows

for adsorbate-adsorbate interactions. kMC simulations have a much higher computational cost than the mean-field model, however, it allows for a more realistic treatment of the systems. In our study, CHA is not an infinitely surface, and the distribution of active sites is not random, which makes it interesting to perform kMC simulations. The kMC simulation in this work is developed with the first reaction method [106] and operated through a Python program, MonteCoffee. [102]

The kMC approach accounts for the probability of a system to be in a certain state and the time evolution of the system is studied by considering the chemical master equation:

$$\frac{dP_\alpha}{dt} = \sum_\beta [k_{\alpha\beta}P_\beta - k_{\beta\alpha}P_\alpha] \tag{4.3}$$

P_α is the probability of the system to be in state α and P_β is the probability of the system to be in state β. The transition between states is given by the rate constant $k_{\alpha\beta}$ ($\alpha \rightarrow \beta$) and $k_{\beta\alpha}$ ($\beta \rightarrow \alpha$). The rate constant is calculated by the change in entropy and energy between the initial and transition states following eq. (3.7).

Before performing kMC, the elementary steps of the reaction, which are the events in kMC, and their rate constants need to be defined. Based on the proposed mechanism, the considered events are selected and stored in an event list. With an event list containing rate constants, the first reaction method can be used. The algorithm is summarized in Fig. 4.1. The six steps of the first reaction method are below.
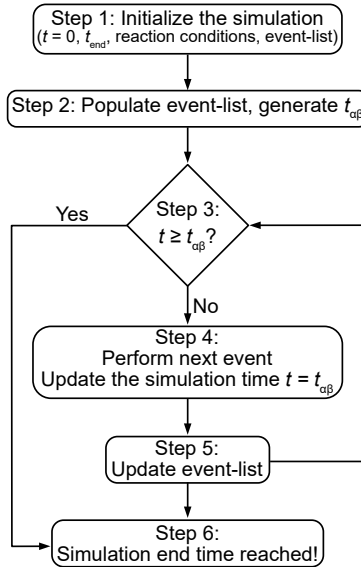

Figure 4.1: Illustration of the algorithm for the first reaction method that applied in kinetic Monte Carlo simulation.

Step 1: The kMC simulation is initialized in this step by setting the initial time $t = 0$ and the end time of the simulation t_{end}. An event-list that includes the possible processes

is created to keep track of the events, their time of occurrence, and the site where the events proceed. The list will be updated at each simulation step.

Step 2: This step is to generate the occurrence time and populate the event-list of all the possible events. Accordingly, the time of occurrence ($t_{\beta\alpha}$) for the event in the first reaction method can be obtained by:

$$t_{\beta\alpha} = t - \frac{1}{k_{\beta\alpha}}\ln u \tag{4.4}$$

where u is a random uniform number between [0,1], and $k_{\beta\alpha}$ is the rate constant.

Step 3: Determine whether the time has reached the end time ($t \geq t_{\beta\alpha}$).

Step 4: Perform the next reaction in chronological order within the event-list. If this reaction is impossible to occur, discard it and proceed to the next possible event.

Step 5: Once the step is executed, the event-list will be updated, including new events that have been enabled. It is worth noting that only the events that happen in the neighborhood around the site where the last step occurred are updated. In this way, the large consumption of computational resources associated with global updating can be avoided.

Step 6: The end time is reached and the simulation is ended. Since a large amount of data is generated during the kMC simulation, unnecessary information is cleaned up, and required data is saved during the computation to minimize memory consumption.

As the method is based on random numbers, the simulation will usually run for long times and averages are taken over many trajectories. By analyzing the TOF obtained at different temperatures, kMC simulation can also yield activation energies of the reaction. In addition, due to being based on specific sites, kMC simulations provide information on where the reactions preferentially occur.

4.3 Developing a kinetic model

It is worth noting that a reasonable kinetic model needs to be validated and improved based on experimental measurements rather than get there in one step. Fig. 4.2 illustrates the workflow that was applied during the construction of our microkinetic model. The
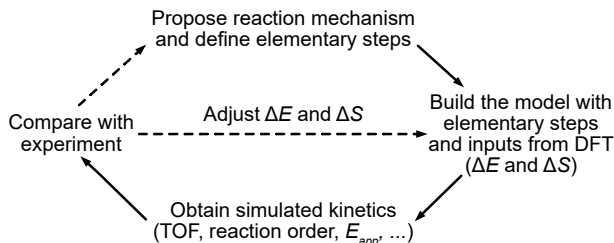

Figure 4.2: Illustration of the workflow for constructing a microkinetic model based on first principles calculations.

reaction mechanism was established according to experiments and DFT calculations, which

provided the elementary steps as well as the changes in energy and entropy. Through the elementary steps and inputs (ΔE, ΔS), rate constants, apparent activation energy, reaction order, and other kinetic parameters can be obtained. The validity of the kinetic model needs to be verified by comparing experimental and simulated kinetic parameters. If the kinetic results from the model are significantly different, the mechanism and inputs should be corrected based on the experiment as in some steps there may be inaccuracy due to the limitations of the DFT simulation itself. After that, the next round of equation solving and kinetic parameter calculations should be performed for the comparison with the experimental data until the agreement is reached. For the low-temperature model of NH_3-SCR over Cu-CHA, four iterations were needed to achieve a sufficient agreement.

4.4 Analysis of reaction kinetics

As mentioned above, one of the major roles of kinetic models is to provide kinetic results that can be compared with experimental measurements, and in this way, validate proposed reaction paths. This section will focus on the kinetic observables that can be generated and the analysis that can be performed by having a microkinetic model.

4.4.1 Turnover frequency and coverage

Experimentally, the turnover frequency (TOF) is defined as the number of reactant molecules that are converted over one site per second. [90] [(p.174)] In the mean-field kinetic models, TOF can be obtained by summing up the rate of elementary steps that generate the product molecule. For a kMC simulation, TOF can be calculated by the number of reactions that occur per unit time and active site. Generally, there could be a difference in numerical values between the absolute experimental and simulated TOFs due to the sensitivity of the kinetic parameters and experimental issues defining the number of active sites. However, the TOF obtained in a reasonable kinetic model should be consistent with the experimental results in terms of the trends when changing the reaction conditions, such as temperature and reactant concentration. A reasonable model should describe the evolution of the TOF as the temperatures and pressures are changed.

It is worth noting that TOF is not the only criterion to judge catalyst efficiency. The selectivity is also of importance. In the kinetic model, side reactions that produce by-products can be added and the selectivity of the target product is the ratio of product yield to the TOF of the reactant. By comparing the selectivity of experiments and simulations, it is possible to judge whether the reaction mechanism is reasonable or not. On the other hand, when a proper model has been established, it is also possible to assist in the improvement of selectivity to the target product in the experiment by investigating which kinetic parameters affect the selectivity.

In the mean-field model, coverage of each potential species could be obtained directly by solving eq. (4.1) and the coverage should sum up to the saturating coverage, which is one. The comparison between the simulated most abundant species and experimental spectroscopy measurement also helps to judge the validity of the model. Another relevant application of the simulated coverage is to obtain fractions of active sites in different oxidation states during redox reactions. In experiments, the oxidation states can be

measured, for example, by high-energy-resolution fluorescence-detected X-ray absorption near edge structure (HERFD-XANES).[107] By comparing the fractions change with temperature, the proposed reaction mechanism can be evaluated.

4.4.2 Reaction order and apparent activation energy

Reaction orders and apparent activation energy are commonly used to characterize catalytic reactions in both experimental and computational studies. The reaction order reflects the relationship between the concentrations of reactants and the rate of a reaction. Based on the rate equation,[90 (p.38-41)] the relationship between rate r, rate constant k, and the concentration of the gas phase reactants can be expressed as:

$$r = k \prod_i p_i^{n_i} \tag{4.5}$$

where p_i is the partial pressure of species i and n_i is the reaction order of i. In both experiments and simulations, the reaction order of reactant i can be evaluated by studying the variation of reaction rate (or TOF) at a certain pressure gradient of i when the pressure of the other reactants remains constant. A positive reaction order implies that the reactant is positively correlated to the rate of the reaction, while the opposite is observed for a negative reaction order. In other words, with higher pressure of a reactant with a negative reaction order, the reaction is more difficult to carry out. A proposed reaction mechanism can be evaluated by comparing simulated reaction orders with experiments.

For the apparent activation energy, it can be calculated following the Arrhenius equation. By combining eq. (3.5) and eq. (4.5), the following equation is obtained:

$$r = A \exp\left(-\frac{E_{app}}{k_{\mathrm{B}}T}\right) \prod_i p_i^{n_i} \tag{4.6}$$

In experiments, the natural logarithm is generally taken for the reaction rate at different temperatures to plot $\ln r$ vs. $1/T$ as shown in Fig. 4.3. Within a narrow temperature range, the plot of $\ln r$ vs $1/T$ is close to a straight line, and the slope is equal to $-E_{app}/k_{\mathrm{B}}$, which provides the apparent activation energy. The simulated apparent activation energy
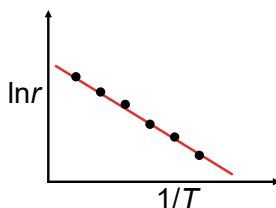

Figure 4.3: Schematic of an Arrhenius plot, yielding the apparent activation energy as the slope.

can be obtained in the same way. It is worth noting that to get a reasonable comparison, the temperature intervals taken should be consistent with the experiment.

4.4.3 Degree of rate control

With a successful model that agrees well with experimental catalytic characters, it is desirable to further analyze the effect of each elementary step on the overall reaction. To achieve this, the degree of rate control (χ_i) analysis is performed to understand the extent to which a particular elementary step determines the simulated catalytic rate. [108;109] The χ_i for each elementary step can be calculated by:

$$\chi_i = \frac{k_i}{r} \left(\frac{\partial TOF}{\partial k_i} \right)_{K_i} \tag{4.7}$$

Here k_i is the rate constant of step i and K_i is the equilibrium constant. The analysis is carried out by changing the value of rate constants for the forward and backward reaction for each elementary step by a small amount (1% in this thesis) while keeping the equilibrium constant and the rate constants of all the other steps constant. The sum of χ_i for a single branch reaction should be one. The value of χ shows the relative importance of each elementary step and the step that has the largest χ can be considered as the rate-determining step at the investigated reaction conditions. With changes in temperature and pressure, the degree of rate control of each elementary step could change as well as the rate-determining step. In this way, this analysis can provide more detailed information about the reaction kinetics from the theoretical side, which can help to experimentally obtain higher activity or selectivity by controlling the reaction conditions.

Chapter 5

Microkinetic model for NH$_3$-SCR over Cu-CHA

Experimental measurement combined with simulated phase diagrams (Fig. 5.1) provide evidence that the NH$_3$-SCR reaction mechanism over Cu-CHA is likely to be different at various temperatures. At low temperatures, the Cu ions in CHA are in the form of [Cu(NH$_3$)$_2$]$^+$, and the NO conversion rate reaches its peak at about 300 °C. With increasing temperatures, [Cu(NH$_3$)$_2$]$^+$ complexes start to decompose into framework [Cu(NH$_3$)]$^+$, and meanwhile, the conversion rate is also decreased and reaches the minimum at about 350 °C. After that, NO conversion increases again when Cu is bound to the framework without any NH$_3$ ligands. Another indication of different reaction mechanisms at low and high temperatures is the N$_2$O selectivity. At low temperatures, the selectivity of N$_2$O is increased with high Cu loading and reaches a peak at about 250 °C and shows a similar trend as NO conversion, while at high temperatures the production of N$_2$O is low. Therefore, it is reasonable to hypothesize that the occurrence of the minimum, or so
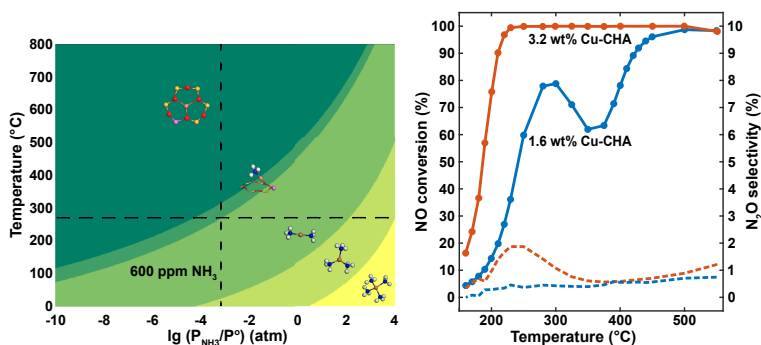

Figure 5.1: Left: The phase diagram of [Cu(NH$_3$)$_x$]$^+$ (x = 0-4) in CHA under varying NH$_3$ pressure and temperature. The horizontal and vertical dashed lines represent 270 °C and 600 ppm NH$_3$ pressure, respectively. Right: NO conversion (solid lines) and N$_2$O formation (dashed lines) versus temperature for standard NH$_3$-SCR over the 1.6 wt % Cu-CHA (blue) and 3.2 wt % Cu-CHA (red) samples.

to speak the "seagull" profile, and the formation of N$_2$O is related to altered reaction mechanisms due to changes in the state of Cu.

In this chapter, we first discuss a mechanism for N$_2$O formation (**Paper I**), which we proposed to have a low barrier over [Cu$_2$(NH$_3$)$_4$O$_2$]$^{2+}$. To investigate the kinetics of

low-temperature NH_3-SCR over Cu-CHA and explore ways to promote the activity as well as selectivity to N_2, a first principles microkinetic model including N_2O formation was developed (**Paper II**). Based on the detailed microkinetic model, a simplified model with only 5 steps was built (**Paper III**). To investigate the proposed model with the Cu-diffusion treated explicitly, a kinetic Monte Carlo approach was applied (**Paper V**). In the last part, a more complete picture of NH_3-SCR and the origin of the "seagull" profile was investigated based on the mechanism for high-temperature NH_3-SCR (**Paper IV**).

5.1 N_2O formation during NH_3-SCR at low temperatures

According to the proposed reaction cycles (see Ref. 40 and Fig. 5.2), the low-temperature NH_3-SCR reaction starts with O_2 adsorption over $[Cu(NH_3)_2]^+$ pairs forming a Cu-peroxo species, $[Cu_2(NH_3)_4O_2]^{2+}$. Following that, NO and NH_3 react over the Cu-peroxo yielding H_2NNO and a $[Cu_2(NH_3)_4OOH]^{2+}$ complex (reaction 4 in Fig. 5.2). The H_2NNO intermediate diffuses to Brønsted acid site and decomposes into N_2 and H_2O with the assistance of ammonium (NH_4^+). According to the similar onset temperature of N_2 and
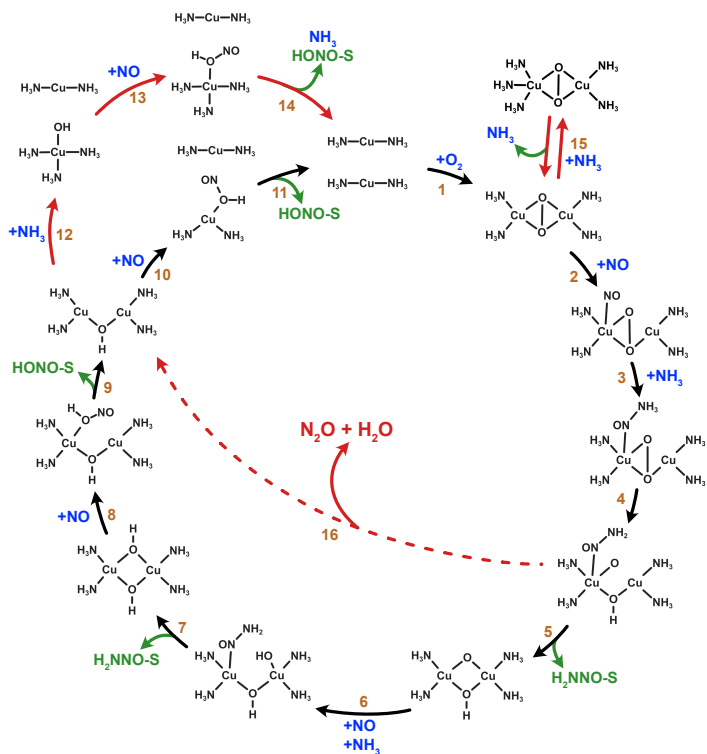

Figure 5.2: Proposed reaction cycle for low-temperature NH_3-SCR over Cu-CHA.

N$_2$O formation in NH$_3$-SCR measurements, it is reasonable to suppose that there can be an N$_2$O formation path that occurs over the same active site as N$_2$ with a similar reaction barrier.

In **Paper I**, the decomposition of the H$_2$NNO intermediate over [Cu$_2$(NH$_3$)$_4$OOH]$^{2+}$ was investigated. It was found that once the first H$_2$NNO forms, the protons on H$_2$NNO can easily transfer to the -OOH group of [Cu$_2$(NH$_3$)$_4$OOH]$^{2+}$ generating N$_2$O, which competes with the diffusion of H$_2$NNO to Brønsted acid site forming N$_2$ and H$_2$O. This reaction path involves spin-flip processes due to the changes in the oxidation state over the Cu cations. If the spin state of Cu is allowed to change along the reaction, this path is barrierless as the path with the dashed line shown in Fig. 5.3(b).
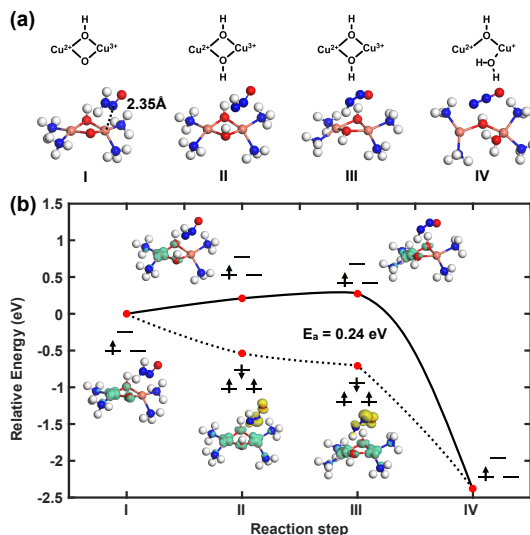

Figure 5.3: (a) Structures of key configurations in the N$_2$O formation over a [Cu(NH$_3$)$_2$-OOH-(CuNH$_3$)$_2$]$^{2+}$ complex and (b) the corresponding reaction landscape. The spin configurations are schematically shown by arrows in (b). The two lower states refer to the two Cu atoms, whereas the single upper state refers to the electronic state of the adsorbate (H$_2$NNO, HNNO, or N$_2$O). The formal charges on the Cu-ions following the least stable potential energy curve (solid line) are shown in (a). The molecular structures in (b) show the spin density at an iso-surface of 0.09 e/Å^3. Atomic color codes: H (white), N (blue), O (red), and Cu (bronze).

However, such a spontaneous reaction would result in a very high selectivity to N$_2$O during the NH$_3$-SCR reaction, which disagrees with experiments. An activation barrier of 0.24 eV is instead calculated if the spin along the reaction is constrained. N$_2$O and H$_2$O are generated after the sequential proton transfers and the Cu active goes to [Cu$_2$(NH$_3$)$_4$OH]$^{2+}$, which is also a species that appears within the reaction cycles. Therefore, this N$_2$O formation path can be coupled to the original reaction cycle as a side reaction as reaction 16 in Fig. 5.2), and provide a possibility for calculating the selectivity of N$_2$O from the kinetic model.

5.2 Microkinetic model for low-temperature NH$_3$-SCR

Based on the proposed reaction cycle (marked by black arrows in Fig. 5.2) and the N$_2$O formation path (marked by red dashed arrow in Fig. 5.2), a microkinetic model of low-temperature NH$_3$-SCR was developed, and the analysis of the reaction kinetics was performed to compare with experimental results. It is important to note that in the microkinetic model, the fractional coverages are understood as the fractions of Cu-site that are in a certain state within the reaction cycle.

The used ΔE and ΔS were all from DFT calculations in the first version of our microkinetic model. However, these values resulted in an extremely low fractional coverage of Cu-peroxo complexes. Experimentally,[47;105] it has been showed that O$_2$ adsorb on [Cu(NH$_3$)$_2$]$^+$ is possible. To improve the model and achieve a better agreement with the experiments, different attempts and corrections were made to the model.

5.2.1 Correction of the underestimated O$_2$ adsorption energy

The low fractional coverage of Cu-peroxo originates from the underestimated adsorption energy of O$_2$ (0.2 eV) in the DFT calculations. To improve the kinetic model, the reported experimental value of 0.82 eV in Ref. 105 was adopted as a correction. The difference of O$_2$ adsorption energy between calculated and experimental can be attributed to the difficulty describing properly O$_2$ in the gas phase with the exchange-correlation that is applied in this work as well as the arbitrariness of the initial state for the [Cu(NH$_3$)$_2$]$^+$ pairs.

By adopting the experimental value for O$_2$ adsorption, this elementary step was conducted at a reasonable forward reaction rate and the subsequent steps in this second version model were able to proceed. However, the light-off measurements and reaction orders for this model still do not agree with experimental light-off measurements and reaction orders.

5.2.2 Inclusion of the NH$_3$ blocking step

In experiments with an NH$_3$/NO ratio close to or higher than 1, the reaction order to NH$_3$ is zero or slightly negative, with an apparent activation energy of about 0.4 to 0.8 eV.[19;110] However, the second version of the model gives a positive reaction order (0.05) for NH$_3$ and a relatively low apparent activation barrier of 0.31 eV. These results indicate that NH$_3$ should have a hindering effect on the reaction in the experiment and also raise the apparent activation barrier, which is not accounted for in the model.

Recent experimental work that focuses on the Cu-peroxo complexes observed that excess NH$_3$ can be adsorbed on the Cu-peroxo complexes, leading to a partial reduction of Cu.[111] Related DFT calculations were performed in this thesis and revealed that the extra NH$_3$ on the Cu site of Cu-peroxo (shown in Fig. 5.4) has an adsorption energy of 0.98 eV, which is higher than NO (E$_{ads-NO}$ = 0.70 eV). More importantly, NO is not able to react over this [Cu$_2$(NH$_3$)$_5$(O$_2$)]$^+$ complex, which indicates that the adsorption of the extra NH$_3$ can hinder the NH$_3$-SCR reaction by competing with NO for the active site. Thus, the NH$_3$ adsorption step was added to the reaction cycle (reaction 15 in Fig. 5.2) in the third version of the model. With the hindering effect of NH$_3$, the reaction

order to NH$_3$ reduces to -0.22 and gives an apparent activation energy of 0.75 eV, which is in very good agreement with experiments.
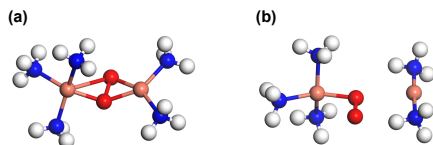

Figure 5.4: Two structures of [Cu$_2$(NH$_3$)$_5$(O$_2$)]$^{2+}$. Atom color codes: Cu (bronze), Si (yellow), Al (pink), O (red), N (blue) and H (white).

The inhibiting-NH$_3$ occupies the Cu-peroxo site and it is thus, only when NH$_3$ desorb from the site that NO can adsorb and the reaction can proceed. Given that the potential energy surface of the proposed reaction mechanism is flat, it is the adsorption energy of the inhibiting-NH$_3$ that determines the reaction rate and mainly contributes to the apparent activation energy.

5.2.3 Consideration of the probability for Cu pairing

With the correction of O$_2$ adsorption energy and the inclusion of the NH$_3$ blocking step, the third version of the microkinetic model already reproduces the experimental kinetic parameters fairly well. However, the calculated TOF, although following the trend of the experimental light-off curve, was significantly overestimated. To close the gap between simulation and experiment, the probability of having a pair of [Cu(NH$_3$)$_2$]$^+$ in the same cage was taken into account. The third kinetic model had a pair of Cu-complexes as a starting point and once O$_2$ has been adsorbed, the sequential elementary steps start. However, as reported in previous work,[47] the pairing process that one [Cu(NH$_3$)$_2$]$^+$ diffuse to another cage that already has a [Cu(NH$_3$)$_2$]$^+$ to form a Cu-complexes pair is endothermic and associated with a barrier. To take the endothermic into account, a factor of 6×10^{-4} was multiplied to the TOF, which corresponds to the equilibrium distribution of the Cu-pairs at 200 °C. In the mean-field kinetic model, this probability is added to obtain a reasonable TOF.

To simulate the nature of mobility of [Cu(NH$_3$)$_2$]$^+$ and stability of [Cu(NH$_3$)$_2$]$^+$ pairs in a more explicit way, kMC approach is introduced in **Paper IV** to model the inhomogeneous properties of CHA. When the stability between paired and unpaired complexes is set to be 0.31 eV, which corresponds to a situation with one Al in each cage,[47] the kMC model provided a very similar conversion curve as in the mean-field kinetic model with an apparent activation energy of 0.79 eV (0.75 eV in the mean-field kinetic model). By raising the stability of [Cu(NH$_3$)$_2$]$^+$ pairs, the turnover frequencies increase from 0.25 s^{-1} to 30 s^{-1}, while the apparent activation energy reduces slightly from 0.79 eV to 0.64 eV. The kMC study in this work revealed that the different apparent activation energies in experiments with the same Cu loading could be partly due to different synthesis methods resulting in varying Al-distributions.[110;112;113]

5.2.4 Reaction order and the effect of O_2

The experimental fits over the reaction order measurements for 1.6 wt% Cu-CHA sample and the TOFs evaluated from the first principles microkinetic model are shown in Fig. 5.5. The TOFs from the model are simulated with reaction conditions similar to those in experiments for reaction order measurements. The comparisons show a very good
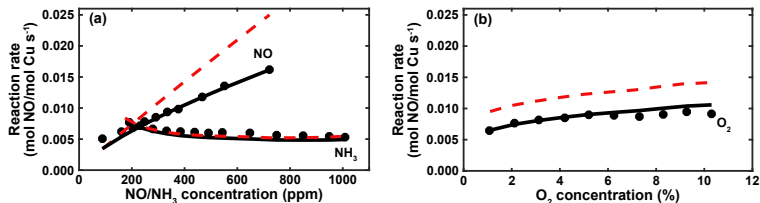
Figure 5.5: Experimental reaction rate (black dots) over the 1.6 wt% Cu-CHA sample and simulated TOFs (red dashed line) versus the concentration of (a)NO, NH_3, and (b) O_2 at 200 °C. The experiment data is provided by Xueting Wang from the Competence Centre for Catalysis at Chalmers, and the experiment details are given in **Paper II**.

agreement between experiments and our final mean-field model on both the reaction orders and reaction rates, especially for NH_3. For oxygen, the trend is consistent, although the rates are slightly overestimated in the simulations. For the simulated TOF of NO, it agrees at low NO concentrations but starts to divide with increasing concentrations. We attribute this overestimation to the lack of possible side reactions in the model that consumes NO without producing any N_2. Nevertheless, the experimental and computational TOFs are within a factor of 2, which confirms the validity of this model.

The reaction order to O_2 has been measured to be reduced with increasing O_2 pressure.[114] A series of simulations with Cu/Al ratio of 0.23, which is the same as in the experiment were conducted and shown in Fig. 5.6, where the blue line is the simulation result and the orange dots are from experimental measurement. The results show that
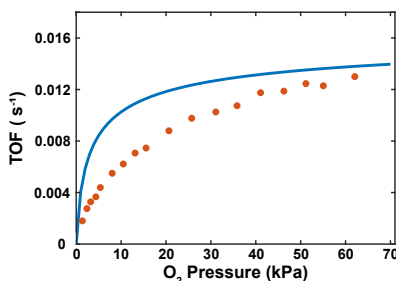
Figure 5.6: Turnover frequency of NO consumption over Cu-CHA with a Cu/Al ratio of 0.23 using the cycle in Fig. 5.2 (solid line). The experiments (dots) are taken from Ref. 114. The simulations and experiments are performed at a temperature of 473 K with partial pressures of NO and NH_3 being both 0.03 kPa.

our kinetic model closely follows the experimental trend while the simulated rate at low pressures increases steeper than the experiment. The results indicate that at low temperatures the formation of the peroxo species could be overestimated as in experiments not all the Cu are involved.

5.2.5 The effect of Cu/Al ratio

The successful development of the microkinetic model has allowed the prediction of experimental observations from the model. Our model can be used for the rational design of new catalysts. One of the issues that has received attention is the effect of Cu/Al ratio on the selectivity of N_2O. In the proposed reaction cycle, the selectivity of N_2O is based on the probability of the reaction following reaction 5 or reaction 16. Moreover, as the NH_3-SCR reaction requires both the Cu sites and Brønsted acid sites, while N_2O formation only needs the Cu sites, the selectivity of N_2O should be affected by the Cu/Al ratio. In the model, the original Cu/Al ratio was set to 0.5 which gives an N_2O selectivity of 4 % at 250 °C. To investigate the effect of Cu/Al ratio, simulations with different ratios were performed, and the N_2O productions are shown in Fig. 5.7. When the Cu/Al ratio decreases, selectivity also shows a decreasing trend which matches the experimental observation. In the case of a Cu/Al ratio equal to 0.33, it is close to the experimental sample with 1.6% of Cu loading and both have about 2% selectivity of N_2O at 250°C.
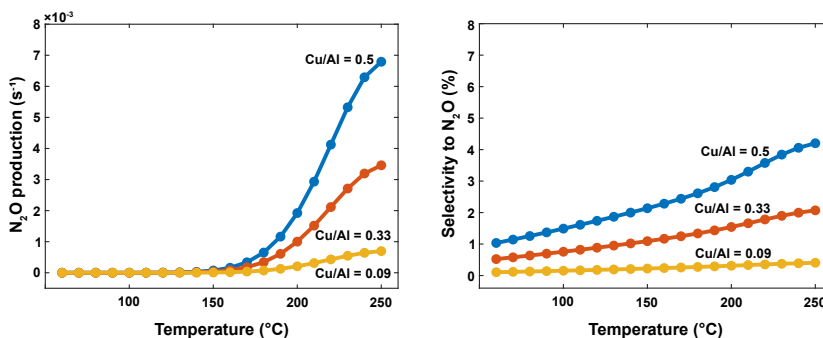

Figure 5.7: Simulated N_2O production (left) and selectivity (right) over Cu-CHA with different Cu/Al ratios.

5.3 Microkinetic model for high-temperature NH_3-SCR

With increasing temperatures, the mobile $[Cu(NH_3)_2]^+$ complexes, which are critical for the low-temperature mechanism, will decompose into framework-bound Cu species, and thus, no longer allow the reaction process to follow the same reaction mechanism. Here, the NH_3-SCR reaction over framework-bound Cu is investigated.

The first explored pathway was to perform the reaction over two framework-bound Cu in similarity with the low-temperature mechanism. Moreover, the mechanistic study

of methane-to-methanol conversion over framework-bound Cu-CHA indicated that Cu-dimers are important for O_2 activation.[115] After O_2 adsorbed on two framework-bound Cu, framework-bound Cu-peroxo (Z-CuOOCu-Z) forms. DFT calculation showed that with the Z-CuOOCu-Z site, NH_3 and NO coupling follow a similar path as in the low-temperature reaction cycle, forming N_2, H_2O and the by-product, N_2O, with low barriers. With a lower barrier of N_2O formation than N_2 formation, this path will bring a high yield of N_2O, which is inconsistent with the low N_2O formation observed experimentally at high temperatures. Besides, due to the repulsion between the Cu ions, it was found that the framework Cu-dimer is unlikely to be the dominant configuration, which results in difficulty in the adsorption of O_2 and the formation of Z-CuOOCu-Z.

Since the Cu-dimer mechanism did not agree with the experimental observation, we proposed a reaction mechanism with one framework Cu ion. With the co-adsorption of NO and O_2 on the framework Cu, $ZCu[NO_3]^+$ can be formed and further reaction with NO forming $ZCu[NO_2]^+$ and gas phase NO_2. After the adsorption of another NO, NH_3 can react with $ZCu[NO_2-NO]^+$ generating H_2NNO and HONO, which will further convert into N_2 and H_2O as shown in Fig. 5.8. As the resting state of the catalyst after synthesis can be ZCu^+, ZCu^{2+}, and $ZCu[OH^-]^{2+}$, the proposed mechanism also included the conversion of Cu^{2+} to Cu^+ and the possible path of starting with $Cu[OH^-]^{2+}$. The highest barrier in the path is located in the formation of $ZCu[NO_2]^+$, which require to overcome a barrier of 1.10 eV. The adsorption energy of NH_3 on ZCu^+ is 1.35 eV, which
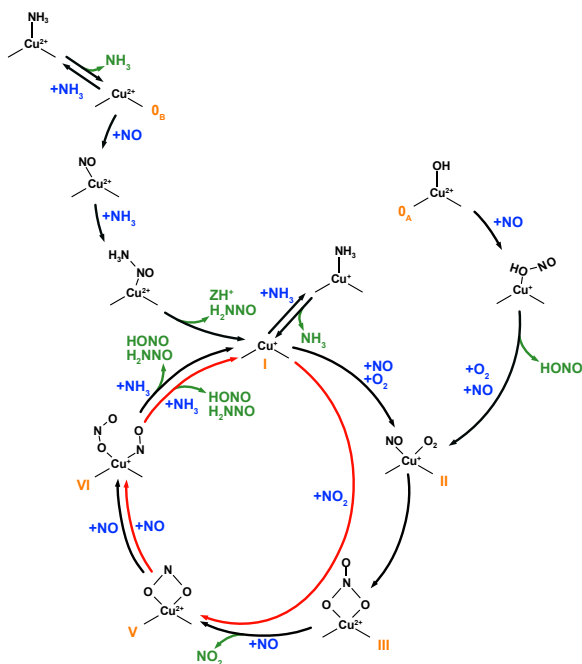

Figure 5.8: Proposed reaction cycle for high-temperature NH_3-SCR over one framework bound Cu-ions.

was considered as the limiting step for the high-temperature SCR reaction. It is worth noting that $[Cu(NH_3)]^+$ is the dominant species at 270 to 310 °C when the concentration of NH_3 is 600 ppm as shown in the simulated phase diagram in Fig. 5.1.

5.4 Origin of the "seagull" profile in NH$_3$-SCR over Cu-CHA

With the proposed reaction mechanism for low- and high-temperature NH$_3$-SCR, it is possible to reproduce the "seagull" profile of experimental NO conversion. Here, we use the probabilities of Cu-ions in the form of $[Cu(NH_3)_2]^+$ or $[Cu(NH_3)]^+$ at different temperatures to connect the reaction mechanisms. The probability of the reaction proceeding via low-temperature mechanism $P(LT)$ is given by:

$$P(LT) = \frac{1}{1 + e^{-\Delta G/k_B T}} \tag{5.1}$$

Where ΔG is the Gibbs free energy difference at a specified NH$_3$ pressure between $[Cu(NH_3)_2]^+$ and $Z[Cu\text{-}NH_3]^+$ with one NH$_3$ molecule in the gas phase. The probability of the reaction proceeding via high-temperature, $P(HT)$, can calculate by 1-$P(LT)$. Following that, the TOF of NH$_3$-SCR over the entire temperature interval is:

$$\text{TOF}_{total} = \text{TOF}_{LT} \times P(LT) + \text{TOF}_{HT} \times P(HT) \tag{5.2}$$

Here, the TOF_{LT} and TOF_{LT} are calculated based on the low- and high-temperature mechanism from the mean-field microkinetic model, respectively. Considering the limitation of accuracy in DFT calculation, the original TOF from DFT was fitted with the experimental NO$_x$ conversion to correct the key parameter of the rate-determining step, which is at low temperatures the NH$_3$ desorption from a $[Cu_2(NH_3)_5O_2]^{2+}$ complex[113] and NH$_3$ desorption from $Z[Cu\text{-}NH_3]^+$ at the high-temperature model. The fitting suggests that adjustments of 0.10 eV and +10 J/mol · K for the low-temperature mechanism and -0.02 eV and -3 J/mol · K for the high-temperature mechanism on the energy and entropy difference are needed. With the corrections, our simulated TOF can reproduce the "seagull" profile and it agrees well with the experimental NO$_x$ conversion (Fig. 5.9).
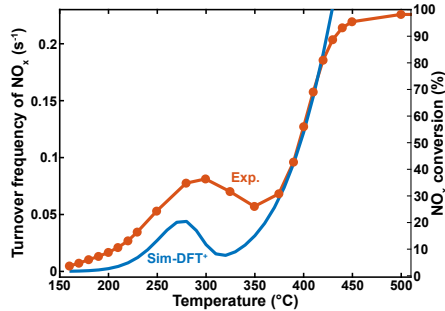

Figure 5.9: Simulated turnover frequency and experimental NO$_x$ conversion of NH$_3$-SCR over Cu-CHA from 150 to 500 °C.

Having reaction models for both the low- and high-temperature NH_3-SCR reaction, we have a full picture of the measured NO_x conversion. From 150 °C to the first peak, NH_3 that block on the $[Cu_2(NH_3)_5O_2]^{2+}$ complexes desorb, which enables the NH_3-SCR reaction. After that, the coverage of O_2 becomes low on the $[Cu(NH_3)_2]^+$ pairs and the $[Cu(NH_3)_2]^+$ complexes start to decompose, which results in the decrease of SCR activity. Meanwhile, the high-temperature mechanism begins to gain in importance; however, it is limited by the NH_3 adsorption on ZCu. Both mechanisms are difficult to carry out at intermediate temperatures, resulting in the formation of the "seagull" minimum. Once the fraction of ZCu site increases with higher temperatures, the high-temperature mechanism will dominate and, allowing the SCR activity to increase again.

Chapter 6

Conclusions and outlook

The main aim of this thesis was to investigate the reaction kinetics of NH_3-SCR over Cu-CHA by establishing first principles microkinetic models. To achieve this aim, different attempts have been made to refine the previously proposed reaction mechanism and evaluate the entropy. After several iterations, our models achieved good agreement with the experiment and provided new insights for further understanding of NH_3-SCR over Cu-CHA. Depending on the difference in active sites as a function of temperature, the reaction mechanism study has been divided into low- and high-temperature parts.

For the low-temperature NH_3-SCR, an N_2O formation path that can be coupled in the multi-site mechanism was proposed. The low reaction barrier and the critical role of Cu-site for the proposed path explained the nearly simultaneous emission peaks of N_2 and N_2O that were observed in experiments.

Following that, a first principles mean-field microkinetic model was developed. To obtain rate constants that can reflect the actual situation of the elementary steps, detailed estimations of the entropy were performed. The simulation of NH_3-TPD was introduced to assist in determining the accuracy of evaluated entropies. By fitting to experimental NH_3-TPD, the validity of the methods used to estimate entropy was confirmed. A similar method was used to evaluate the entropy loss of O_2 adsorption over $[Cu(NH_3)_2]^+$ pairs, which agrees well with experimental measurement. Through comparisons with experiments, our model was revised by adopting the experimental adsorption energy of O_2, adding the NH_3 inhibition effect, and considering the possibility of having a pair of $Cu(NH_3)_2$ complexes in the same cage. The final version of the model reached a good agreement with the experimental kinetics.

By comparing the models with the presence and absence of inhibiting-NH_3, the significant impact of NH_3 on the NH_3-SCR was revealed. The analysis of coverage and the degree of rate control further uncovered how the inhibiting NH_3 determines the onset temperature of NH_3-SCR. With the model, it can be concluded that the low-temperature mechanism contains NH_3 with different roles:

1. Ligand-NH_3: NH_3 that adsorbs on the Cu-cations, forming mobile $[Cu(NH_3)_2]^+$ complexes, which enable the facile formation of pairs for O_2 adsorption. The ligand-NH_3 does not participate in the low-temperature SCR reaction provided that NH_3 is in excess.

2. Inhibiting-NH_3: NH_3 that adsorbs strongly on the $[Cu_2(NH_3)_4O_2]^{2+}$ species, and thereby blocks the adsorption of NO, which is required for NH_3 SCR reaction.

3. Reactant-NH_3: NH_3 that takes part in the reaction by reacting with NO.

4. NH_4^+: NH_3 that is adsorbed at the Brønsted acid sites forming NH_4^+.

In low-temperature NH_3-SCR, NH_3 acts simultaneously as a reactant, spectator, and inhibitor. It is nearly impossible to obtain such information by experiment alone, showing the significance and necessity of developing microkinetic models. In addition, the kinetic model revealed that the NH_3-SCR and the formation of N_2O are coupled, both react over the Cu sites, making it difficult to completely limit N_2O formation. However, since the conversation of H_2NNO and HONO relies on Brønsted acid site, increasing the amount of Brønsted acid site while keeping Cu loading will help improve selectivity to N_2. To speed up the calculation and focus on the critical steps, a simplified model with only five steps is developed from the full microkinetic model. By treating the adsorption of O_2, NH_3, and NO explicitly with lumped reactions for N_2 and N_2O formation, the simplified model described the reaction kinetics accurately.

To treat the diffusion and pairing of $[Cu(NH_3)_2]^+$ complexes at low-temperature NH_3-SCR in an explicit way for investing the effect of the Al-distribution on the reaction kinetics, a kinetic Monte Carlo model was developed. The model revealed that Al-distribution can affect the stability of $[Cu(NH_3)_2]^+$ pairs and the adsorption competition between NH_3 and NO adsorption on $[Cu_2(NH_3)_4O_2]^{2+}$ complex. The link between structural properties and catalytic performance provides direction for further improvement of NH_3-SCR catalyst.

When shifting to the high-temperature interval, Cu exists in the form of framework-bound Cu. Here a study of reaction mechanisms and microkinetic modeling were performed to investigate high-temperature NH_3-SCR. It showed that at high temperatures, the NH_3-SCR proceeds over one framework-bound Cu ions by a different mechanism than at low temperatures. NH_3 is also in the high-temperature mechanism both a reactant and an inhibitor. $Z[Cu(NH_3)]^+$ is one of the potential states in the phase diagram, which is also the blocking state of high-temperature NH_3-SCR. By linking the low- and high-temperature mechanisms, the DFT-based reaction models were able to reproduce the measured "seagull" profile in NO conversion and provide a reasonable explanation of this phenomenon.

This work greatly deepened the understanding of NH_3-SCR over Cu-CHA from the atomic level, which is expected to facilitate the improvement of activity and selectivity to N_2 in practical applications. In subsequent studies, attempts can be made to integrate the results from the kinetic model into the reactor model and explore the kinetics at larger scales, which would guide the rational design of catalysts. In addition, there are experiments showing that water affects the activity and the selectivity of the NH_3-SCR, which is not considered in our model but could be a topic for future studies. With very high operation temperatures and high water concentrations, the dealumination process begins to occur and deactivates the catalyst. To increase the duration of the catalyst and to maintain its activity, mechanism research in this field is also of significant importance.

The new generation of vehicles is being powered by cleaner biodiesel, hydrogen, and fuel cells, but this does not mean this work will lose its application. Alterations in fuel composition will result in changes in emission composition, which places different demands on the operating range of the catalysts. The research methods and workflow that are developed in this work are general and can be used to accelerate the pace of research with heterogeneous catalysis.

Acknowledgments

In addition, I would like to thank:

My main supervisor, Henrik Grönbeck. Thank you for always answering my questions patiently, giving me advice to find my way, and get back on track. I appreciate your guidance, listening, and encouragement!

My co-supervisors, Magnus Skoglundh, and Anders Hellman for the discussions and encouragement at all the presentations.

All colleagues in the FFI project, for all the discussion and support. I have learned so much from working with you guys and I am glad we have accomplished so much together!

All my colleagues at Chemical Physics and KCK are gratefully acknowledged. Thank you for creating a warm and nice working environment (and the best fika). I appreciate that here I can always ask for help and raise questions!

I would also like to especially thank Lin for the discussion on NH_3-SCR and Rasmus for the help in running Monte Coffee. Without your help, I would have had to spend a lot more time to push my project forward.

All my Chinese friends in Goteborg for always encouraging me and taking me out.

Jesper and the Samsioe family (including Bosse and Sprak), for always standing by my side and giving me lots of support! And, of course, my mum and dad, it would be impossible for me to go this far without your support. Thank you so much for loving me enough to let me free and do whatever I want.

Yingxin Feng, Göteborg, January 2024

Bibliography

[1] Nørskov, J. K.; Bligaard, T.; Rossmeisl, J.; and Christensen, C. H. Towards the Computational Design of Solid Catalysts. *Nat. Chem.*, *1* (2009), 37–46. doi: 10.1038/nchem.121.

[2] Twigg, M. V. Progress and Future challenges in Controlling Automotive Exhaust Gas Emissions. *Appl. Catal. B Environ.*, *70* (2007), 2–15. doi: 10.1016/j.apcatb.2006.02.029.

[3] Sourses of Air Polution in Europe. [EB/OL]. `https://www.eea.europa.eu/themes/air/air-pollution-sources-1`.

[4] Lashof, D. A. and Ahuja, D. R. Relative Global Warming Potentials of Greenhouse Gas Emissions. *Nature*, *344* (1990), 529–531.

[5] [EB/OL]. `https://www.dieselforum.org/about-clean-diesel/what-is-scr/`.

[6] Emissions of Air Pollutants from Transport. [EB/OL]. `https://www.eea.europa.eu/data-and-maps/indicators/transport-emissions-of-air-pollutants-8/transport-emissions-of-air-pollutants-8`.

[7] Johnson, T. V. Diesel Emission Control in Review. *SAE Tech. Pap.*, *1* (2001), 68–81. doi: 10.4271/2001-01-0184.

[8] Seinfeld, J. H. Air Pollution: A Half Century of Progress. *AIChE J.*, *50* (2004), 1096–1108. doi: 10.1002/aic.10102.

[9] European Emission Standards. [EB/OL]. `https://eur-lex.europa.eu/legal-content/EN/TXT/?uri=CELEX:02011R0582-20191215#E0017`.

[10] Belton, D. N. and Taylor, K. C. Automobile Exhaust Emission Control by Catalysts. *Curr. Opin. Solid State Mater. Sci.*, *4* (1999), 97–102. doi: 10.1016/S1359-0286(99)80017-5.

[11] Bosteels, D. and Searles, R. A. Exhaust Emission Catalyst Technology. *Platin. Met. Rev.*, *46* (2002), 27–36.

[12] Pereda-Ayo, B. and González-Velasco, J. R. *Diesel Engine - NO_x Storage and Reduction for Diesel Engine Exhaust Aftertreatment.* IntechOpen, Rijeka, 2013. doi: 10.5772/55729.

[13] Kašpar, J.; Fornasiero, P.; and Hickey, N. Automotive: Catalytic Converters Current Status and Some Perspectives. *Catal. Today*, *77* (2003), 419–449.

[14] Nova, I. and Tronconi, E. *Urea-SCR Technology for $DeNO_x$ After Treatment of Diesel Exhausts.* Springer Science+Business Media New York, 2014.

[15] Chorkendorff, I. and Niemantsverdriet, J. W. *Concepts of Modern Catalysis and Kinetics*. John Wiley & Sons, 2017.

[16] Dumesic, J. A.; Huber, G. W.; and Boudart, M. Principles of Heterogeneous Catalysis. In Handbook of Heterogeneous Catalysis. (2008), 1–26. doi: 10.1002/9783527610044.hetcat0001. URL https://doi.org/10.1002/9783527610044.hetcat0001.

[17] Parshall, G. W. Industrial applications of homogeneous catalysis. A review. *J. Mol. Catal.*, *4* (1978), 243–270. doi: https://doi.org/10.1016/0304-5102(78)85023-8. URL https://www.sciencedirect.com/science/article/pii/0304510278850238.

[18] Yang, X.-F.; Wang, A.; Qiao, B.; Li, J.; Liu, J.; and Zhang, T. Single-Atom Catalysts: A New Frontier in Heterogeneous Catalysis. *Acc. Chem. Res.*, *46* (2013), 1740–1748. doi: 10.1021/ar300361m. URL https://doi.org/10.1021/ar300361m.

[19] Gao, F.; Mei, D.; Wang, Y.; Szanyi, J.; and Peden, C. H. Selective Catalytic Reduction over Cu/SSZ-13: Linking Homo- and Heterogeneous Catalysis. *J. Am. Chem. Soc.*, *139* (2017), 4935–4942. doi: 10.1021/jacs.7b01128.

[20] Chen, F.; Jiang, X.; Zhang, L.; Lang, R.; and Qiao, B. Single-Atom Catalysis: Bridging the Homo- and Heterogeneous Catalysis. *Chinese J. Catal.*, *39* (2018), 893–898. doi: 10.1016/S1872-2067(18)63047-5. URL http://dx.doi.org/10.1016/S1872-2067(18)63047-5.

[21] Forzatti, P. Present Status and Perspectives in De-NO_x SCR Catalysis. *Appl. Catal. A Gen.*, *222* (2001), 221–236. doi: 10.1016/S0926-860X(01)00832-8.

[22] Chen, B. and Kan, H. Air Pollution and Population Health: A Global Challenge. *Environ. Health Prev. Med.*, *13* (2008), 94–101. doi: 10.1007/s12199-007-0018-5.

[23] Grossale, A.; Nova, I.; Tronconi, E.; Chatterjee, D.; and Weibel, M. NH_3-NO/NO_2 SCR for Diesel Exhausts Aftertreatment: Reactivity, Mechanism and Kinetic Modelling of Commercial Fe- and Cu-Promoted Zeolite Catalysts. *Top. Catal.*, *52* (2009), 1837–1841. doi: 10.1007/s11244-009-9354-6.

[24] Xin, Y.; Li, Q.; and Zhang, Z. Zeolitic Materials for $DeNO_x$ Selective Catalytic Reduction. *ChemCatChem*, *10* (2018), 29–41. doi: 10.1002/cctc.201700854.

[25] Jeon, J.; Lee, J. T.; and Park, S. Nitrogen Compounds (NO, NO_2, N_2O, and NH_3) in NO_x Emissions from Commercial EURO VI Type Heavy-Duty Diesel Engines with a Urea-Selective Catalytic Reduction System. *Energy and Fuels*, *30* (2016), 6828–6834. doi: 10.1021/acs.energyfuels.6b01331.

[26] Pérez-Ramírez, J.; Kapteijn, F.; Schöffel, K.; and Moulijn, J. A. Formation and Control of N_2O in Nitric Acid Production: Where Do We Stand Today? *Appl. Catal. B Environ.*, *44* (2003), 117–151. doi: 10.1016/S0926-3373(03)00026-2.

[27] Liu, B.; Yao, D.; Wu, F.; Wei, L.; Li, X.; and Wang, X. Experimental Investigation on N_2O Formation during the Selective Catalytic Reduction of NO_x with NH_3 over Cu-SSZ-13. *Ind. Eng. Chem. Res.*, *58* (2019), 20516–20527. doi: 10.1021/acs.iecr.9b03294.

[28] Emissions in the automotive sector. https://single-market-economy.ec.europa.eu/sectors/automotive-industry/environmental-protection/emissions-automotive-sector_en.

[29] Colombo, M.; Nova, I.; and Tronconi, E. Detailed Kinetic Modeling of the NH_3-NO/NO_2 SCR Reactions over a Commercial Cu-Zeolite Catalyst for Diesel Exhausts After Treatment. *Catal. Today*, *197* (2012), 243–255. doi: 10.1016/j.cattod.2012.09.002. URL http://dx.doi.org/10.1016/j.cattod.2012.09.002.

[30] Ciardelli, C.; Nova, I.; Tronconi, E.; Chatterjee, D.; Bandl-Konrad, B.; Weibel, M.; and Krutzsch, B. Reactivity of NO/NO_2-NH_3 SCR System for Diesel Exhaust Aftertreatment: Identification of the Reaction Network as a Function of Temperature and NO_2 feed content. *Appl. Catal. B Environ.*, *70* (2007), 80–90. doi: 10.1016/j.apcatb.2005.10.041.

[31] Chaturvedi, S. and Dave, P. N. Review on Thermal Decomposition of Ammonium Nitrate. *J. Energ. Mater.*, *31* (2013), 1–26. doi: 10.1080/07370652.2011.573523.

[32] Babrauskas, V. and Leggett, D. Thermal Decomposition of Ammonium Nitrate. *Fire Mater.*, *44* (2020), 250–268. doi: 10.1002/fam.2797.

[33] Chen, H. Y.; Wei, Z.; Kollar, M.; Gao, F.; Wang, Y.; Szanyi, J.; and Peden, C. H. A Comparative Study of N_2O Formation during the Selective Catalytic Reduction of NO_x with NH_3 on Zeolite Supported Cu Catalysts. *J. Catal.*, *329* (2015), 490–498. doi: 10.1016/j.jcat.2015.06.016. URL http://dx.doi.org/10.1016/j.jcat.2015.06.016.

[34] Zhang, D. and Yang, R. T. N_2O Formation Pathways over Zeolite-Supported Cu and Fe Catalysts in NH_3-SCR. *Energy Fuels*, *32* (2018), 2170–2182. doi: 10.1021/acs.energyfuels.7b03405.

[35] Kröcher, O. and Elsener, M. Chemical Deactivation of V_2O_5/WO_3-TiO_2 SCR Catalysts by Additives and Impurities from Fuels, Lubrication Oils, and Urea Solution. I. Catalytic Studies. *Appl. Catal. B Environ.*, *77* (2008), 215–227. doi: 10.1016/j.apcatb.2007.04.021.

[36] Englund, J.; Dahlin, S.; Schaefer, A.; Xie, K.; Andersson, L.; Shwan, S.; Carlsson, P. A.; Pettersson, L. J.; and Skoglundh, M. Deactivation of a Vanadium-Based SCR Catalyst Used in a Biogas-Powered Euro VI Heavy-Duty Engine Installation. *Catalysts*, *10* (2020). doi: 10.3390/catal10050552.

[37] Schildhauer, T. J.; Elsener, M.; Moser, J.; Begsteiger, I.; Chatterjee, D.; Rusch, K.; and Kröcher, O. Measurement of Vanadium Emissions from SCR Catalysts by

ICP-OES: Method Development and First Results. *Emiss. Control Sci. Technol.*, *1* (2015), 292–297. doi: 10.1007/s40825-015-0023-x.

[38] Schmieg, S. J.; Oh, S. H.; Kim, C. H.; Brown, D. B.; Lee, J. H.; Peden, C. H.; and Kim, D. H. Thermal Durability of Cu-CHA NH_3-SCR Catalysts for Diesel NO_x Reduction. *Catal. Today*, *184* (2012), 252–261. doi: 10.1016/j.cattod.2011.10.034.

[39] Davis, M. E. and Lobo, R. F. Zeolite and Molecular Sieve Synthesis. *Chem. Mater.*, *4* (1992), 756–768. doi: 10.1021/cm00022a005.

[40] Chen, L.; Janssens, T. V.; Vennestrøm, P. N.; Jansson, J.; Skoglundh, M.; and Grönbeck, H. A Complete Multisite Reaction Mechanism for Low-Temperature NH_3-SCR over Cu-CHA. *ACS Catal.*, *10* (2020), 5646–5656. doi: 10.1021/acscatal.0c00440.

[41] Brandenberger, S.; Kröcher, O.; Tissler, A.; and Althoff, R. *The State of the Art in Selective Catalytic Reduction of NO_x by Ammonia Using Metal-Exchanged Zeolite Catalysts*, volume 50. 2008. ISBN 0161494080. doi: 10.1080/01614940802480122.

[42] Kwak, J. H.; Tonkyn, R. G.; Kim, D. H.; Szanyi, J.; and Peden, C. H. Excellent Activity and Selectivity of Cu-SSZ-13 in the Selective Catalytic Reduction of NO_x with NH_3. *J. Catal.*, *275* (2010), 187–190. doi: 10.1016/j.jcat.2010.07.031. URL `http://dx.doi.org/10.1016/j.jcat.2010.07.031`.

[43] Beale, A. M.; Gao, F.; Lezcano-Gonzalez, I.; Peden, C. H.; and Szanyi, J. Recent Advances in Automotive Catalysis for NO_x Emission Control by Small-Pore Microporous Materials. *Chem. Soc. Rev.*, *44* (2015), 7371–7405. doi: 10.1039/c5cs00108k.

[44] Fickel, D. W.; D'Addio, E.; Lauterbach, J. A.; and Lobo, R. F. The Ammonia Selective Catalytic Reduction Activity of Copper-Exchanged Small-Pore Zeolites. *Appl. Catal. B Environ.*, *102* (2011), 441–448. doi: 10.1016/j.apcatb.2010.12.022. URL `http://dx.doi.org/10.1016/j.apcatb.2010.12.022`.

[45] Blakeman, P. G.; Burkholder, E. M.; Chen, H. Y.; Collier, J. E.; Fedeyko, J. M.; Jobson, H.; and Rajaram, R. R. The Role of Pore Size on the Thermal Stability of Zeolite Supported Cu SCR Catalysts. *Catal. Today*, *231* (2014), 56–63. doi: 10.1016/j.cattod.2013.10.047. URL `http://dx.doi.org/10.1016/j.cattod.2013.10.047`.

[46] Gao, F.; Kwak, J. H.; Szanyi, J.; and Peden, C. H. Current Understanding of Cu-exchanged Chabazite Molecular Sieves for Use as Commercial Diesel Engine $DeNO_x$ Catalysts. *Top. Catal.*, *56* (2013), 1441–1459. doi: 10.1007/s11244-013-0145-8.

[47] Paolucci, C.; Khurana, I.; Parekh, A. A.; Li, S.; Shih, A. J.; Li, H.; Iorio, J. R. D.; Albarracin-caballero, J. D.; Yezerets, A.; Miller, J. T.; Delgass, W. N.; Ribeiro, F. H.; Schneider, W. F.; and Gounder, R. Dynamic Multinuclear Sites Formedby Mobilized Copper Ions in NOx Selective Catalytic Reduction. *Science*, *357* (2017), 898–903.

[48] Akter, N.; Chen, X.; Parise, J.; Boscoboinik, J. A.; and Kim, T. Effects of Copper Loading on NH_3-SCR and NO Oxidation over Cu Impregnated CHA Zeolite. *Korean J. Chem. Eng.*, *35* (2018), 89–98. doi: 10.1007/s11814-017-0268-x.

[49] Yao, D.; Li, Y.; Liu, B.; Hu, X.; and Wu, F. Mechanism-Based Kinetic Modeling of N_2O Formation on SCR Activity over Cu-SSZ-13 Catalysts for Diesel Vehicle. *Appl. Catal. A Gen.*, *648* (2022), 118915. doi: 10.1016/j.apcata.2022.118915. URL `https://doi.org/10.1016/j.apcata.2022.118915`.

[50] Feng, Y. Reaction Kinetics of NH_3-SCR over Cu-CHA from First Principles. *Licentiate thesis*, page Chalmers University of Technology. URL `http://proxy.lib.chalmers.se/login?url=https://www.proquest.com/dissertations-theses/reaction-kinetics-nh-sub-3-scr-over-cu-cha-first/docview/2637678885/se-2`.

[51] Dirac, P. A. M. Quantum Mechanics of Many-electron Systems. *Proceedings of the Royal Society of London. Series A, Containing Papers of a Mathematical and Physical Character*, *123* (1929), 714–733.

[52] Schrödinger, E. An Undulatory Theory of the Mechanics of Atoms and Molecules. *Phys. Rev.*, *28* (1926), 1049–1070. doi: 10.1103/PhysRev.28.1049. URL `https://link.aps.org/doi/10.1103/PhysRev.28.1049`.

[53] Born, M. and Oppenheimer, R. J. On the Quantum Theory of Molecules (English translation). *Ann. Phys.*, *457* (1927), 1–32. URL `http://www.ulb.ac.be/cpm/people/scientists/bsutclif/bornop.pdf`.

[54] Hohenberg, P. and Kohn, W. Inhomogeneous Electron Gas. *Phys. Rev.*, *136* (1964), B864–B871. doi: 10.1103/PhysRev.136.B864. URL `https://link.aps.org/doi/10.1103/PhysRev.136.B864`.

[55] Cohen, A. J.; Mori-Sánchez, P.; and Yang, W. Challenges for Density Functional Theory. *Chem. Rev.*, *112* (2012), 289–320. doi: 10.1021/cr200107z.

[56] Kohn, W. and Sham, L. J. Self-Consistent Equations Including Exchange and Correlation Effects. *Phys. Rev.*, *140* (1965), A1133–A1138. doi: 10.1103/PhysRev.140.A1133. URL `https://link.aps.org/doi/10.1103/PhysRev.140.A1133`.

[57] Sousa, S. F.; Fernandes, P. A.; and Ramos, M. J. General Performance of Density Functionals. *J. Phys. Chem. A*, *111* (2007), 10439–10452. doi: 10.1021/jp0734474.

[58] Perdew, J. P.; Ruzsinszky, A.; Tao, J.; Staroverov, V. N.; Scuseria, G. E.; and Csonka, G. I. Prescription for the Design and Selection of Density Functional Approximations: More Constraint Satisfaction with Fewer Fits. *J. Chem. Phys.*, *123* (2005). doi: 10.1063/1.1904565.

[59] Perdew, J. P. and Schmidt, K. Jacob's Ladder of Density Functional Approximations for the Exchange-Correlation Energy. *AIP Conference Proceedings*, *577* (2001), 1–20. doi: 10.1063/1.1390175. URL `https://doi.org/10.1063/1.1390175`.

[60] Kurth, S.; Perdew, J. P.; and Blaha, P. Molecular and Solid-State Tests of Density Functional Approximations: LSD, GGAs, and Meta-GGAs. *Int. J. Quantum Chem.*, *75* (1999), 889–909. doi: 10.1002/(SICI)1097-461X(1999)75:4/5¡889::AID-QUA54¿3.0.CO;2-8.

[61] Dirac, P. A. Note on Exchange Phenomena in the Thomas Atom. *Math. Proc. Cambridge Philos. Soc.*, *26* (1930), 376–385. doi: 10.1017/S0305004100016108.

[62] Ceperley, D. M. and Alder, B. J. Ground State of the Electron Gas by a Stochastic Method. *Phys. Rev. Lett.*, *45* (1980), 566–569. doi: 10.1103/PhysRevLett.45.566. URL https://link.aps.org/doi/10.1103/PhysRevLett.45.566.

[63] Perdew, J. P. and Zunger, A. Self-Interaction Correction to Density-Functional Approximations for Many-Electron Systems. *Phys. Rev. B*, *23* (1981), 5048–5079. doi: 10.1103/PhysRevB.23.5048. URL https://link.aps.org/doi/10.1103/PhysRevB.23.5048.

[64] Perdew, J. P.; Burke, K.; and Ernzerhof, M. Generalized Gradient Approximation Made Simple. *Phys. Rev. Lett.*, *77* (1996), 3865–3868. doi: 10.1103/PhysRevLett.77.3865.

[65] Gross, E. K. and Dreizler, R. M. Gradient Expansion of the Coulomb Exchange Energy. *Zeitschrift für Phys. A Atoms Nucl.*, *302* (1981), 103–106. doi: 10.1007/BF01413038.

[66] Adamo, C.; Ernzerhof, M.; and Scuseria, G. E. The Meta-GGA Functional: Thermochemistry With a Kinetic Energy Density Dependent Exchange-Correlation Functional. *J. Chem. Phys.*, *112* (2000), 2643–2649. doi: 10.1063/1.480838.

[67] Bao, J. L.; Gagliardi, L.; and Truhlar, D. G. Self-Interaction Error in Density Functional Theory: An Appraisal. *J. Phys. Chem. Lett.*, *9* (2018), 2353–2358. doi: 10.1021/acs.jpclett.8b00242.

[68] Harvey, J. N. On the Accuracy of Density Functional Theory in Transition Metal Chemistry. *Annu. Reports Prog. Chem. - Sect. C*, *102* (2006), 203–226. doi: 10.1039/b419105f.

[69] Krukau, A. V.; Vydrov, O. A.; Izmaylov, A. F.; and Scuseria, G. E. Influence of the Exchange Screening Parameter on the Performance of Screened Hybrid Functionals. *J. Chem. Phys.*, *125* (2006). doi: 10.1063/1.2404663.

[70] Borlido, P.; Aull, T.; Huran, A. W.; Tran, F.; Marques, M. A.; and Botti, S. Large-Scale Benchmark of Exchange-Correlation Functionals for the Determination of Electronic Band Gaps of Solids. *J. Chem. Theory Comput.*, *15* (2019), 5069–5079. doi: 10.1021/acs.jctc.9b00322.

[71] Anisimov, V. I.; Zaanen, J.; and Andersen, O. K. Band Theory and Mott Insulators: Hubbard U instead of Stoner I. *Phys. Rev. B*, *44* (1991), 943–954. doi: 10.1103/PhysRevB.44.943.

[72] Chen, L.; Janssens, T. V.; and Grönbeck, H. A Comparative Test of Different Density Functionals for Calculations of NH_3-SCR over Cu-Chabazite. *Phys. Chem. Chem. Phys.*, *21* (2019), 10923–10930. doi: 10.1039/c9cp01576k.

[73] Isseroff, L. Y. and Carter, E. A. Importance of Reference Hamiltonians Containing Exact Exchange for Accurate One-Shot GW Calculations of Cu_2O. *Phys. Rev. B - Condens. Matter Mater. Phys.*, *85* (2012), 1–7. doi: 10.1103/PhysRevB.85.235142.

[74] Lundqvist, B. I.; Andersson, Y.; Shao, H.; Chan, S.; and Langreth, D. C. Density Functional Theory Including Van Der Waals Forces. *Int. J. Quantum Chem.*, *56* (1995), 247–255. doi: https://doi.org/10.1002/qua.560560410. URL https://onlinelibrary.wiley.com/doi/abs/10.1002/qua.560560410.

[75] Shukla, V.; Jiao, Y.; Lee, J.-H.; Schröder, E.; Neaton, J. B.; and Hyldgaard, P. Accurate Nonempirical Range-Separated Hybrid van der Waals Density Functional for Complex Molecular Problems, Solids, and Surfaces. *Phys. Rev. X*, *12* (2022), 041003.

[76] Shukla, V.; Jiao, Y.; Frostenson, C. M.; and Hyldgaard, P. VdW-DF-Ahcx: a Range-Separated Van Der Waals Density Functional Hybrid. *J. Phys.: Condens. Matter*, *34* (2022), 025902.

[77] Grimme, S.; Antony, J.; Ehrlich, S.; and Krieg, H. A Consistent and Accurate Ab Initio Parametrization of Density Functional Dispersion Correction (DFT-D) for the 94 Elements H-Pu. *J. Chem. Phys.*, *132* (2010), 154104. doi: 10.1063/1.3382344.

[78] Blöchl, P. Projector Augmented-Wave Method. *Phys. Rev. B.*, *50* (1994), 17953–17979. doi: 10.1103/PhysRevB.50.17953.

[79] Sattler, K. D. *DFT Calculations of Vibrational Frequencies*, chapter 3, pages 3–2. Taylor Francis Group, 2010. ISBN 9781420075403. doi: 10.1016/s1369-7021(11)70037-2.

[80] Kresse, G. and Furthmüller, J. Efficiency of Ab-Initio Total Energy Calculations for Metals and Semiconductors using a Plane-Wave Basis Set. *Comput. Mater. Sci.*, *6* (1996), 15–50. doi: 10.1016/0927-0256(96)00008-0.

[81] Kresse, G. and Hafner, J. Ab Initio Molecular Dynamics for Open-Shell Transition Metals. *Phys. Rev. B - Condens. Matter Mater. Phys.*, *48* (1993), 13115–13118. doi: 10.1103/PhysRevB.48.13115.

[82] Schlegel, H. B. Geometry Optimization. *Wiley Interdiscip. Rev. Comput. Mol. Sci.*, *1* (2011), 790–809. doi: 10.1002/wcms.34.

[83] Schlegel, H. B. Geometry Optimization. *Wiley Interdiscip. Rev. Comput. Mol. Sci.*, *1* (2011), 790–809. doi: 10.1002/wcms.34.

[84] Teter, M. P.; Payne, M. C.; and Allan, D. C. Solution of Schrödingers Equation for Large Systems. *Phys. Rev. B*, *40* (1989), 12255–12263. doi: 10.1103/PhysRevB.40.12255.

[85] *Ab Initio Molecular Dynamics*, chapter 9, pages 193–208. John Wiley & Sons, Ltd, 2009. ISBN 9780470447710. doi: https://doi.org/10.1002/9780470447710.ch9. URL `https://onlinelibrary.wiley.com/doi/abs/10.1002/9780470447710.ch9`.

[86] Verlet, L. Computer "Experiments" on Classical Fluids. I. Thermodynamical Properties of Lennard-Jones Molecules. *Phys. Rev.*, *159* (1967), 98–103. doi: 10.1103/PhysRev.159.98. URL `https://link.aps.org/doi/10.1103/PhysRev.159.98`.

[87] Koch, W. and Holthausen, M. C. *A Chemist's Guide to Density Functional Theory.* John Wiley & Sons, 2015.

[88] Karhánek, D. VASP Infrared Intensities, July 2020. doi: 10.5281/zenodo.3930989. URL `https://doi.org/10.5281/zenodo.3930989`.

[89] *DFT Calculations of Vibrational Frequencies*, chapter 5, pages 113–130. John Wiley & Sons, Ltd, 2009. ISBN 9780470447710. doi: https://doi.org/10.1002/9780470447710.ch5. URL `https://onlinelibrary.wiley.com/doi/abs/10.1002/9780470447710.ch5`.

[90] Chorkendorff, I. and Niemantsverdriet, J. W. *Concepts of Modern Catalysis and Kinetics.* WILEY-VCH Verlag GmbH & Co. KGaA, Weinheim, second, revised and enlarged edition, 2007.

[91] Henkelman, G. and Jónsson, H. Improved Tangent Estimate in the Nudged Elastic Band Method for Finding Minimum Energy Paths and Saddle Points. *J. Chem. Phys.*, *113* (2000), 9978–9985. doi: 10.1063/1.1323224.

[92] Henkelman, G.; Uberuaga, B. P.; and Jónsson, H. A Climbing Image Nudged Elastic Band Method for Finding Saddle Points and Minimum Energy Paths. *The Journal of Chemical Physics*, *113* (2000), 9901–9904. doi: 10.1063/1.1329672. URL `https://doi.org/10.1063/1.1329672`.

[93] Tang, W.; Sanville, E.; and Henkelman, G. A Grid-based Bader Analysis Algorithm Without Lattice Bias. *J. Phys. Condens. Matter*, *21* (2009), 084204. doi: 10.1088/0953-8984/21/8/084204.

[94] Sanville, E.; Kenny, S. D.; Smith, R.; and Henkelman, G. Improved Grid-Based Algorithm for Bader Charge Allocation. *Journal of Computational Chemistry*, *28* (2007), 899–908. doi: https://doi.org/10.1002/jcc.20575. URL `https://onlinelibrary.wiley.com/doi/abs/10.1002/jcc.20575`.

[95] Lomachenko, K. A.; Borfecchia, E.; Negri, C.; Berlier, G.; Lamberti, C.; Beato, P.; Falsig, H.; and Bordiga, S. The Cu-CHA DeNO$_x$ Catalyst in Action: Temperature-Dependent NH$_3$-Assisted Selective Catalytic Reduction Monitored by Operando XAS and XES. *J. Am. Chem. Soc.*, *138* (2016), 12025–12028. doi: 10.1021/jacs.6b06809.

[96] Chen, L.; Falsig, H.; Janssens, T. V.; and Grönbeck, H. Activation of Oxygen on (NH$_3$–Cu–NH$_3$)$^+$ in NH$_3$-SCR over Cu-CHA. *J. Catal.*, *358* (2018), 179–186. doi: 10.1016/j.jcat.2017.12.009.

[97] Gould, H. and Tobochnik, J. *Statistical and Thermal Physics With Computer Applications.* Princeton University Press, Woodstock, Oxfordshire, 2010. P 318.

[98] Ochterski, J. W. and Ph, D. Thermochemistry in Gaussian. *Gaussian Inc Pittsburgh PA*, *264* (2000), 1–19.

[99] Larsen, A. H.; Mortensen, J. J.; Blomqvist, J.; Castelli, I. E.; Christensen, R.; Dułak, M.; Friis, J.; Groves, M. N.; Hammer, B.; Hargus, C.; Hermes, E. D.; Jennings, P. C.; Jensen, P. B.; Kermode, J.; Kitchin, J. R.; Kolsbjerg, E. L.; Kubal, J.; Kaasbjerg, K.; Lysgaard, S.; Maronsson, J. B.; Maxson, T.; Olsen, T.; Pastewka, L.; Peterson, A.; Rostgaard, C.; Schiøtz, J.; Schütt, O.; Strange, M.; Thygesen, K. S.; Vegge, T.; Vilhelmsen, L.; Walter, M.; Zeng, Z.; and Jacobsen, K. W. The Atomic Simulation Environment—a Python Library for Working with Atoms. *Journal of Physics: Condensed Matter*, *29* (2017), 273002. URL http://stacks.iop.org/0953-8984/29/i=27/a=273002.

[100] Bahn, S. R. and Jacobsen, K. W. An Object-Oriented Scripting Interface to a Legacy Electronic Structure Code. *Comput. Sci. Eng.*, *4* (2002), 56–66. doi: 10.1109/5992.998641.

[101] Jørgensen, M. and Grönbeck, H. Adsorbate Entropies with Complete Potential Energy Sampling in Microkinetic Modeling. *J. Phys. Chem. C*, *121* (2017), 7199–7207. doi: 10.1021/acs.jpcc.6b11487.

[102] Jørgensen, M. and Grönbeck, H. MonteCoffee: A programmable kinetic Monte Carlo framework. *J. Chem. Phys.*, *149* (2018). doi: 10.1063/1.5046635. URL http://dx.doi.org/10.1063/1.5046635.

[103] Niwa, M.; Katada, N.; Sawa, M.; and Murakami, Y. Temperature-Programmed Desorption of Ammonia with Readsorption Based on the Derived Theoretical Equation. *J. Phys. Chem.*, *99* (1995), 8812–8816. doi: 10.1021/j100021a056.

[104] Katada, N.; Igi, H.; Kim, J. H.; and Niwa, M. Determination of the Acidic Properties of Zeolite by Theoretical Analysis of Temperature-Programmed Desorption of Ammonia Based on Adsorption Equilibrium. *J. Phys. Chem. B*, *101* (1997), 5969–5977. doi: 10.1021/jp9639152.

[105] Wang, X.; Chen, L.; Vennestrøm, P. N.; Janssens, T. V.; Jansson, J.; Grönbeck, H.; and Skoglundh, M. Direct Measurement of Enthalpy and Entropy Changes in NH_3 Promoted O_2 Activation over Cu-CHA at Low Temperature. *ChemCatChem*, *13* (2021), 2577–2582. doi: 10.1002/cctc.202100253.

[106] Henning, T. *An introduction to Kinetic Monte Carlo Simulations of surface reactions*, volume 815. Springer, 2010. ISBN 9783642132582.

[107] Fahami, A. R.; Günter, T.; Doronkin, D. E.; Casapu, M.; Zengel, D.; Vuong, T. H.; Simon, M.; Breher, F.; Kucherov, A. V.; Brückner, A.; and Grunwaldt, J. D. The Dynamic Nature of Cu Sites in Cu-SSZ-13 and the Origin of the Seagull NO_x Conversion Profile during NH_3-SCR. *React. Chem. Eng.*, *4* (2019), 1000–1018. doi: 10.1039/c8re00290h.

[108] Campbell, C. T. Future Directions and Industrial Perspectives Micro- and Macro-kinetics: Their Relationship in Heterogeneous Catalysis. *Topics in Catalysis*, *1* (1994), 353–366. doi: 10.1007/BF01492288.

[109] Stegelmann, C.; Andreasen, A.; and Campbell, C. T. Degree of Rate Control: How Much the Energies of Intermediates and Transition States Control Rates. *J. Am. Chem. Soc.*, *131* (2009), 8077–8082. doi: 10.1021/ja9000097.

[110] Bates, S. A.; Verma, A. A.; Paolucci, C.; Parekh, A. A.; Anggara, T.; Yezerets, A.; Schneider, W. F.; Miller, J. T.; Delgass, W. N.; and Ribeiro, F. H. Identification of the Active Cu Site in Standard Selective Catalytic Reduction with Ammonia on Cu-SSZ-13. *J. Catal.*, *312* (2014), 87–97. doi: 10.1016/j.jcat.2014.01.004. URL `http://dx.doi.org/10.1016/j.jcat.2014.01.004`.

[111] Negri, C.; Selleri, T.; Borfecchia, E.; Martini, A.; Lomachenko, K. A.; Janssens, T. V.; Cutini, M.; Bordiga, S.; and Berlier, G. Structure and Reactivity of Oxygen-Bridged Diamino Dicopper(II) Complexes in Cu-Ion-Exchanged Chabazite Catalyst for NH3-Mediated Selective Catalytic Reduction. *J. Am. Chem. Soc.*, *142* (2020), 15884–15896. doi: 10.1021/jacs.0c06270.

[112] Shih, A. J. Synthesis and Characterization of Copper-Exchanged Zeolite Catalysts and Kinetic Studies on No_x Selective Catalytic Reduction With Ammonia. (2018).

[113] Feng, Y.; Wang, X.; Janssens, T. V. W.; Vennestrøm, P. N. R.; Jansson, J.; Skoglundh, M.; and Grönbeck, H. First-Principles Microkinetic Model for Low-Temperature NH3-Assisted Selective Catalytic Reduction of NO over Cu-CHA. *ACS Catal.*, (2021), 14395–14407. doi: 10.1021/acscatal.1c03973.

[114] Jones, C. B.; Khurana, I.; Krishna, S. H.; Shih, A. J.; Delgass, W. N.; Miller, J. T.; Ribeiro, F. H.; Schneider, W. F.; and Gounder, R. Effects of Dioxygen Pressure on Rates of NO_x Selective Catalytic Reduction with NH_3 on Cu-CHA Zeolites. *J. Catal.*, *389* (2020), 140–149. doi: 10.1016/j.jcat.2020.05.022. URL `https://doi.org/10.1016/j.jcat.2020.05.022`.

[115] Engedahl, U.; Boje, A.; Ström, H.; Grönbeck, H.; and Hellman, A. Complete Reaction Cycle for Methane-to-Methanol Conversion over Cu-SSZ-13: First-Principles Calculations and Microkinetic Modeling. *J. Phys. Chem. C*, *125* (2021), 14681–14688. doi: 10.1021/acs.jpcc.1c04062.